

CHEMICAL EOR PROCESS VISUALIZATION USING NOA81 MICROMODELS

by

Shaken Kenzhekhanov

A thesis submitted to the Faculty and the Board of Trustees of the Colorado School of Mines in partial fulfillment of the requirements for the degree of Master of Science (Petroleum Engineering).

Golden, Colorado

Date \_\_\_\_\_

Signed: \_\_\_\_\_  
Shaken Kenzhekhanov

Signed: \_\_\_\_\_  
Dr. Xiaolong Yin  
Thesis Advisor

Golden, Colorado

Date \_\_\_\_\_

Signed: \_\_\_\_\_  
Dr. Erdal Ozkan  
Professor and Head  
Department of Petroleum

## ABSTRACT

The main goal for all enhanced oil recovery (EOR) processes is to gain additional oil recovery after, or in some cases along primary and secondary recovery methods. For EOR processes that use immiscible displacement to increase oil recovery, the overall displacement efficiency can be increased by improving the mobility ratio or by increasing the capillary number. Core flooding is the traditional method to study the parameters above. However, microfluidic micromodels are causing huge interest from industry. In this study, we developed procedures to fabricate microfluidic porous media micromodels using a novel polymer – Norland Optical Adhesive 81 (NOA81). NOA81 helped to overcome limitations of previous work by Xu et al. (2014) such as crude oil incompatibility and deformation with higher temperatures.

NOA81 micromodels were used to investigate visually the effects of temperature and different wettability on displacement efficiency in water and surfactant flooding. In addition, the natural fractures were introduced in porous media to study water and surfactant flooding in fractured reservoirs. The temperature effect on displacement efficiency demonstrated that increasing the temperature and decreasing interfacial tension (IFT) between fluids results in higher recovery factor and can be well correlated with the capillary number. The presence of connected natural fractures showed no recovery from matrix porous media in water flooding. However, in surfactant flooding 80% oil recovery was achieved due to lowering IFT. The wettability effect demonstrated that the water-wet micromodel produced 15% less than intermediate and oil-wet micromodels in water flooding due to early breakthrough. Meanwhile, surfactant flooding achieved almost equal high recovery in both water-wet and oil-wet surfaces. It was found that after breakthrough takes place, no notable oil recovery obtained in all water flooding experiments. In contrast, surfactant flooding recovered more with more pore volume injected. Oil recovery in both water and surfactant flooding was lower in water-wet fluid displacement.

There are many other interesting phenomena observed during displacement efficiency experiments such as dead-end pore displacement, microemulsion generation and complexity of fluid flow dynamics in porous media.

## TABLE OF CONTENTS

ABSTRACT.....	iii
LIST OF FIGURES .....	vii
LIST OF TABLES .....	x
LIST OF SYMBOLS .....	xi
ACKNOWLEDGEMENTS.....	xii
CHAPTER 1 INTRODUCTION .....	1
1.1 An overview of EOR processes .....	1
1.2 Core flooding .....	3
1.3 Micromodel.....	4
1.4 Organization of the Thesis .....	7
CHAPTER 2 METHODOLOGY .....	9
2.1 Micromodel patterns .....	9
2.2 Fabrication of NOA81 micromodels .....	11
2.3 Experimental setup.....	15
2.4 Micromodel permeability.....	16
2.5 Phase saturations.....	19
CHAPTER 3 NOA81 AND FLUID PROPERTIES.....	23
3.1 NOA81 Properties.....	23
3.2 NOA81 wettability modification .....	24
3.2.1 Water-wet modification .....	24
3.2.2 Oil-wet modification.....	26
3.3 Surface characterization using Fourier transform infrared spectroscopy (FTIR). 27	
3.4 Fluid properties .....	29

3.4.1	Viscosity .....	29
3.4.2	Interfacial tension.....	30
CHAPTER 4	EFFECT OF TEMPERATURE.....	31
4.1	Displacement efficiency at the ambient temperature 20°C.....	31
4.2	Displacement efficiency at a high temperature 80°C .....	33
4.3	Correlating displacement efficiency to capillary number .....	34
4.4	Interesting observations .....	35
4.4.1	Oil-water replacement in dead-end pores .....	35
4.4.2	Microemulsion .....	37
4.4.3	Flow reversal in a network of pores.....	38
4.5	Summary .....	38
CHAPTER 5	EFFECT OF WETTABILITY .....	40
5.1	Displacement in water-wet micromodels.....	40
5.2	Displacement in oil-wet micromodels .....	44
5.3	Summary .....	47
CHAPTER 6	EFFECT OF FRACTURES.....	48
6.1	Homogeneous micromodel .....	49
6.2	Half-fractured micromodel .....	51
6.3	Fully-fractured micromodel .....	53
6.4	Summary .....	55
CHAPTER 7	CONCLUSIONS AND RECOMMENDATIONS .....	56
7.1	Conclusions.....	56
7.2	Limitations .....	57
7.3	Recommendations.....	57

REFERENCES ..... 58

## LIST OF FIGURES

Figure 1.1	Displacement of mineral oil (grey fluid) by water (black fluid) in homogeneous and heterogeneous networks with hydrophilic and hydrophobic walls (Wu et al. 2012). .....	6
Figure 1.2	Typical brine (NaCl 1.5 wt, %, dyed) saturation patterns in different porous media patterns at breakthrough times (Xu et al. 2014). .....	6
Figure 2.1	1500 $\mu\text{m}$ $\times$ 500 $\mu\text{m}$ micromodel .....	10
Figure 2.2	4800 $\mu\text{m}$ $\times$ 1200 $\mu\text{m}$ micromodels. A – Homogeneous; B – Half-fractured; C – Fully-fractured pattern. ....	10
Figure 2.3	Pore throat size, porosity and permeability relationship in sandstones (Nelson 2009). .....	11
Figure 2.4	SEM image of NOA81 micromodel inlet channel – 60° view. ....	12
Figure 2.5	NOA81 micromodel fabrication process. NOA81 to NOA81 oxygen plasma bonding method. ....	13
Figure 2.6	Plasma bonding delamination after 3 hours in crude oil environment. ....	13
Figure 2.7	NOA81 micromodel fabrication process. NOA81 to NOA81 half-curing bonding method. ....	14
Figure 2.8	SEM image of NOA81 channels in porous medium – top view.....	15
Figure 2.9	Schematic of the experimental setup. ....	16
Figure 2.10	Experimental setup.....	16
Figure 2.11	Brine saturated micromodel. Image processing steps: A – raw image; B – sharpened; C – background subtracted; D – converted to binary image. ....	20
Figure 2.12	Image processing at each experimental step. A – empty micromodel; B – water saturation; C – oil saturation; D - water/surfactant flooding. ....	21
Figure 3.1	NOA81 polymer components (Silvestrini et al. 2012) .....	23
Figure 3.2	Water-wet modification. ....	25
Figure 3.3	20X magnification of water-wet micromodel. A – Water flooding; B – Surfactant flooding.....	25

Figure 3.4	Oil-wet modification. ....	26
Figure 3.5	20X magnification of oil-wet micromodel. A – Water flooding; B – Surfactant flooding. ....	26
Figure 3.6	NOA81 FTIR analysis. ....	28
Figure 3.7	IFT measurement results. ....	30
Figure 4.1	Distributions of oil and water phases at breakthrough. Displacement is from right to left. A – Water flooding at breakthrough. B – Surfactant flooding at breakthrough. ....	32
Figure 4.2	Displacement efficiency at ambient temperature. ....	32
Figure 4.3	Reservoir temperature displacement efficiency. A – Water flooding at breakthrough. B – Surfactant flooding at breakthrough. ....	33
Figure 4.4	Oil recoveries at 80°C as functions of PV injected. ....	34
Figure 4.5	Oil recovery factor at breakthrough plotted against the capillary numbers. ....	35
Figure 4.6	Dead-end pore displacement at each 60 second time frame. ....	36
Figure 4.7	The particle rotational movement in inlet channel. ....	36
Figure 4.8	Water-oil displacement patterns at 100 PV. Flow direction is from right to left. A – Water flooding. B – Surfactant flooding. Microemulsions in the inlet and outlet channels are highlighted. ....	37
Figure 4.9	A magnified view (20X) of microemulsion in the outlet channel. ....	37
Figure 4.10	Reversed flow observed at the interface between the inlet channel and the porous medium micromodel. ....	38
Figure 5.1	Waterflooding in water-wet micromodel at 10 PV. A – Raw image; B – Binary image. ....	41
Figure 5.2	Surfactant flooding in water-wet micromodel at 10 PV. A – Raw image; B – Binary image. ....	42
Figure 5.3	Water flooding in water-wet micromodel with degassed crude oil at 10 PV. A – Raw image; B – Binary image. ....	42
Figure 5.4	Surfactant flooding in water-wet micromodel with degassed crude oil at 10 PV. A – Raw image; B – Binary image. ....	43



Figure 5.5	Recovery factor in water-wet micromodel .....	43
Figure 5.6	Water flooding in an oil-wet micromodel at 10 PV. A – Raw image; B – Binary image.....	44
Figure 5.7	Surfactant flooding in an oil-wet micromodel at 10 PV. A – Raw image; B – Binary image.....	45
Figure 5.8	Water flooding in an oil-wet micromodel with degassed crude oil at 10 PV. A – Raw image; B – Binary image.....	45
Figure 5.9	Surfactant flooding in an oil-wet micromodel with degassed crude oil at 10 PV. A – Raw image; B – Binary image.....	46
Figure 5.10	Recovery factor in oil-wet micromodel .....	46
Figure 6.1	Water flooding – Homogeneous pattern. A – Raw image; B – Binary image.....	49
Figure 6.2	Surfactant flooding – Homogeneous micromodel. A – Raw image; B – Binary image.....	50
Figure 6.3	Homogeneous micromodel recovery factor as a function of PV injected. ....	50
Figure 6.4	Waterflooding – Half-fractured pattern. A – Raw image; B – Binary image.....	51
Figure 6.5	Surfactant flooding – Half-fractured pattern. A – Raw image; B – Binary image.....	52
Figure 6.6	Half-fractured micromodel recovery factor as a function of PV injected .....	52
Figure 6.7	Waterflooding – Fully-fractured micromodel. A – Raw image; B – Binary image.....	53
Figure 6.8	Surfactant flooding – Fully-fractured micromodel. A – Raw image; B – Binary image.....	54
Figure 6.9	Fully-fractured micromodel recovery factor as a function of PV injected .....	54

## LIST OF TABLES

Table 1.1	List of one cited micromodel studies of petroleum application.....	8
Table 2.1	Porous media pattern permeability .....	17
Table 2.2	1500 $\mu\text{m}$ x 500 $\mu\text{m}$ micromodel hydraulic resistance .....	19
Table 2.3	4800 $\mu\text{m}$ x 1200 $\mu\text{m}$ micromodel hydraulic resistance .....	19
Table 2.4	Phase saturation calculations based on pixel count .....	22
Table 3.1	Densities and viscosities of crude oil and water at 20°C and 80°C .....	29
Table 4.1	Capillary number .....	35
Table 5.1	IFT and capillary number.....	40
Table 6.1	Capillary number in water and surfactant flooding .....	48

## LIST OF SYMBOLS

Symbol	Definition
$M$	Mobility ratio
$\mu$	Viscosity
$k_r$	Relative permeability
$N_c$	Capillary number
$u$	Interstitial velocity
$\gamma$	Interfacial tension
$Q$	Flow rate
$k$	Permeability
$A$	Cross sectional area
$\Delta p$	Pressure difference
$L$	Length
$D$	Diameter
$\Delta l$	Distance between two marked points on the measuring tube
$\Delta t$	Time interval to pass a distance of $\Delta l$
$h$	Height
$w$	Width
$r_h$	Hydraulic radius
$R_h$	Hydraulic resistance
$RF$	Recovery factor
$S_w$	Water saturation
$S_{wi}$	Irreducible water saturation

## ACKNOWLEDGEMENTS

I would also like to express my deepest appreciation to my advisor Dr. Xiaolong Yin for his support, patience and tremendous help that have led me to the fulfillment of this work.

I also thank my thesis committee members: Dr. Hossein Kazemi, Dr. Keith Neeves and Dr. Hazim H. Abbas for their valuable comments and guidance. I am grateful for Denise Winn-Bower and Joe Chen for helping me with administrative and laboratory tasks during my study at CSM.

I would like to thank Halliburton for financial support. I also appreciate the help and support of my friends at Mines: Yang Guo and Younki Cho.

Finally, and most importantly, I want to give special thanks to my wife, Leila Berikbolova, for her support and motivation to accomplish this work.

## CHAPTER 1

### INTRODUCTION

Oil and gas industry has recognized for many years that the age of “easy oil” is ending. Most of the world's largest producing fields are approaching depletion, and most remaining reserves are considered as difficult-to-recover (Alvarado and Manrique 2010). This reality moves the industry to develop and implement innovative EOR techniques to increase the recovery efficiency.

The objective of this study is to fabricate a micromodel using a novel polymer, Norland Optical Adhesive (NOA81), to overcome the limitations of the previously used micromodel material, poly(dimethylsiloxane) (PDMS), and to investigate the effect of interfacial tension (IFT) and wettability in chemical enhanced oil recovery (EOR) processes. Parameters such as IFT, wettability and viscosity are critical for EOR, because these parameters control the mobility of phases and their trapping conditions in porous media.

In this introductory chapter, EOR processes and two primary means to study EOR processes in laboratory, core flooding and microfluidic micromodels, are briefly reviewed. The previous studies by Wu et al. (2012) and Xu et al. (2014) that have paved the ground for this research are discussed.

#### **1.1 An overview of EOR processes**

EOR processes can be classified into three main categories: thermal, miscible and chemical. In thermal recovery, hot fluids, such as steam or hot water, are injected into the formation to reduce the viscosity of oil to enable its flow. Thermal recovery consists of steam flooding, cyclic steam stimulation, in situ combustion, and their modifications. The main targets of thermal EOR processes are heavy oils.

Miscible gas EOR processes mainly focus on light- and medium-gravity, API gravity between 22.3 and 31.1°, crude oils. Miscibility generated between injected gas and oil causes increases in the oil specific volume, reduction in viscosity, and elimination of interface and interfacial tension between the injected fluid and the crude oil (Green and Willhite 1998).

The objective of Chemical EOR is to use chemical agents to improve the microscopic and macroscopic efficiency of immiscible displacement to increase oil recovery. Here, microscopic displacement efficiency relates to displacement or mobilization of hydrocarbons at the pore scale,

whereas macroscopic displacement efficiency characterizes volumetric displacements at the reservoir scale. In this study, we focus on displacement efficiency on the microscopic (pore) level. Water-oil displacement efficiency can be increased by improving water-oil mobility ratio or by reducing oil-water interfacial tension. Here, mobility ratio is defined as the ratio of displacing fluid mobility to displaced-fluid (oil) mobility. The mobility of a fluid describes how easily the fluid can flow through a porous medium. It is defined as the ratio of the relative permeability and the viscosity (Equation 1.1).

$$M = \frac{k_r}{\mu} \quad (1.1)$$

where  $k_r$  is the relative permeability and  $\mu$  is the viscosity. According to this definition, mobility ratio can be improved by lowering the viscosity of the displaced fluid, by increasing the viscosity of the displacing fluid, by reducing the relative permeability of the displacing fluid, or by increasing the relative permeability of the displaced fluid.

Capillary forces have a great impact on oil recovery efficiency. Strong capillary forces can trap hydrocarbons and result in relatively high residual oil saturation after a displacement. Two quantities are usually used to assess the magnitude of capillary forces. Capillary pressure, a quantity that relates to the static distribution of phases in a porous medium, is defined as the difference between the pressure of the non-wetting phase and the pressure of the wetting phase. Capillary Number, a dimensionless group that describes the ratio between the viscous forces and the capillary forces during dynamic displacement, is defined as

$$N_c = \frac{\mu u}{\gamma} \quad (1.2)$$

where  $\mu$  is the dynamic viscosity of water;  $u$  is the interstitial velocity of water;  $\gamma$  is the IFT between water and oil phases. Experimental data show that as the capillary number increases, residual oil saturation decreases (Green and Willhite 1998). When oil-water interfacial tension is reduced, capillary pressure is lowered, and capillary number increases. Both are beneficial to oil recovery.

There are three main types of chemical EOR methods: polymer, surfactant and alkali flooding. The principal mechanisms of these methods are:

- In surfactant flooding, surfactants are used to reduce IFT significantly, which helps to mobilize oil trapped by capillarity;
- Polymer flooding improves the mobility ratio by increasing the viscosity of the injected fluid;

- Alkali flooding also reduces IFT, but surfactant is formed in situ by reaction of a high pH solution with the crude oil;

Many variations of surfactant/polymer flooding have been developed under different names, including surfactant, micellar, microemulsion and chemical flooding. It is quite common that surfactant, polymer and alkali flooding are combined to use the benefits of all of them. Although such combinations can compensate each other in the effects of absorption, temperature, and salinity, they could also reduce the effectiveness of each chemical (Green and Willhite 1998).

## **1.2 Core flooding**

Most petroleum reservoirs have irreducible water saturations at the beginning of the development, and residual oil saturations to water and surfactant flooding due to immiscible properties of oil and water at the end of development. These residual saturations show that neither phases can be completely displaced from the rock. The irreducible water saturation, therefore, is a critical initial condition that laboratory studies strive to reproduce, and the residual oil saturation is an important parameter for evaluating the potential of a reservoir with regard to water or surfactant flooding.

Many core flooding experiments have shown that residual oil saturation can be reduced by modifying the wettability of rock surface, reducing IFT, or improving the viscosity ratio of fluids. Mungan (1964) did one of the first laboratory experiments to study the effects of wettability and IFT on water flooding on core samples. In the study by Gale and Sandvik (1973), the effects of surfactants and polymers were systematically tested using many core flooding experiments. Then, Cooke et al. (1974) tested alkali-surfactant flooding using core samples. With developments in core-scale characterization technologies, Hempkins et al. (1971) used nuclear magnetic resonance (NMR) and Cromwell et al. (1984) used computed tomography (CT) scanning to visualize displacements in core flooding experiments. Since then, NMR and CT scan have become critical tools for visualization of oil saturations. Recent works by Yousef et al. (2011), and Mirzaei et al. (2015) are examples.

IFT between fluids and wettability of reservoir rocks at reservoir conditions are very complex. Rock surface is very delicate, and quality measurements require good core preservation and preparation steps. Because of these intricacies, core experiments are very time-consuming, and

improper handling could cause contamination that leads to wrong and unrepeatably results (Anderson 1987).

### **1.3 Micromodel**

Carefully designed and executed core flooding experiments can represent most, if not all, reservoir conditions and complexities at the length scale of centimeters to tens of centimeters. They are, therefore, critical components of a petroleum reservoir study and are widely used throughout the industry. However, as mentioned above, they are usually expensive and time-consuming. Due to the opaque nature of the cores, it is especially challenging to visualize the displacement process within the cores. Moreover, some experiments change the condition of the core, making it difficult, if not impossible, to reuse the core. These disadvantages led to demands for simple, transparent and easy-to-fabricate micromodels to imitate rock samples. These micromodels are not developed to replace core experiments. Rather, they can be used as standardized tools to visualize and measure multiphase flows through porous media. Therefore, they are valuable for fundamental studies of multiphase flow through porous media and rapid screening.

One of the first attempts to visualize processes in core sample was made by Chatenever and Calhoun (1952). A study of oil displacement by water was conducted on a glass model packed with graded sand. Then, Childress (1975) used acid-etched micromodels to study oil displacement by an aqueous surfactant solution. When gas EOR technologies firstly emerged, acid-etched glass micromodels were used in several studies to visualize solution gas drive and gas injection (Danesh et al. 1987). Likewise, other EOR methods, such as microbial (Bryant and Douglas 1988), foam flooding (Manlowe and Radke 1990), and surfactant/alkali/polymer flooding (Tong et al. 1998), have also been studied using glass micromodels. All studies mentioned above demonstrated consistent results and provided significant insights into the mechanisms of enhanced oil recovery by direct visualization. However, acid-etched glass micromodels often have lacks in precision and control of geometry, which affects the accuracy and repeatability of measurements. These problems have unfortunately led to notable disconnections with core experiments.

Significant improvements in micromodel fabrication in recent years have offered more opportunities to conduct a broad range of visual analyses on a variety of flow processes. Zeilinger et al. (2003) studied the formation damage by drilling and production fluids. Romero and Kantzas (2007) studied the effect of wettability and pore geometry on performance of foamed gel.



Buchgraber et al. (2011) studied viscous oil displacement by polymer solutions. Molla and Mostowfi (2014) used a microfluidic platform to conduct PVT measurements that provided saturation pressure and phase-volumes with only a few microliters ( $\mu\text{L}$ ) ( $1 \mu\text{L} = 10^{-9} \text{ m}^3$ ) of reservoir fluid sample. Nguyen et al. (2014) tested nanoparticle-stabilized  $\text{CO}_2$ -in-water foam for mobility control. Shokrlu and Babadagli (2015) investigated phase distribution and residual oil development during solvent injections. All studies mentioned above were conducted using glass micromodels. Recent developments in micro- and nanofabrication and rapid prototyping have made it possible to fabricate analogs of real porous media with high precision to simulate individual or collections of pores down to even sub-micron scales (Javadpour and Fisher 2008). Wu et al. (2014) studied optic imaging of two-phase-flow behavior in nanoscale (100 nm) fractures. He et al. (2015) investigated surfactant performance in nano micromodels with pore throat size (300 nm) comparable to the shale formations. Wang et al. (2014) studied impact of nanopore confinement on petroleum gas condensation using 500 nm, 50 nm and 30 nm micromodels.

Kovscek group from Stanford University studied multiphase flow in naturally fractured porous media using silicon etched micromodels (Rangel-German and Kovscek 2006). The group conducted evaluation of polymers displacing viscous oil and compared results to computational fluid dynamics simulation of displacement process (Clemens et al. 2012). The Kovscek group also developed kaolinite coated micromodels to study low salinity water flooding (Song and Kovscek 2015).

Wu et al. (2012) conducted one of the first water flooding experiments at Colorado School of Mines. The objective of the study was to generate complex porous media models for visualization of multiphase flows. The microfluidic device was fabricated using soft-lithography technique using poly(dimethylsiloxane) (PDMS) polymer. The porous media and dimensions were  $5\text{mm} \times 5\text{mm}$  with  $60 \mu\text{m}$  channel height,  $10 \mu\text{m}$  channel width, and porosity of 11%. The authors used a numerical algorithm to generate porous medium based on Voronoi tessellation that provides some level of complexity and randomness comparing to periodic patterns (Figure 1.1). In the experiments, the micromodel was saturated with mineral oil and then was displaced with the brine solution. The authors showed that the wettability is a predominant factor that controls oil displacement by water. In a subsequent study, Xu et al. (2014) studied the effect of geometry and interfacial tension on multiphase displacement (Figure 1.2). Different geometries with identical

porosities were designed to investigate displacement efficiency. The authors concluded that in both water and surfactant flooding, pore size distribution and heterogeneity lower the recovery factor. In multiphase flow experiments, surfactant changes not only the interfacial tension but also the speeds of forced drainage, increasing in capillary number, which implies higher recovery factor. Both Wu et al. (2012) and Xu et al. (2014) used PDMS as the fabrication material, which is not compatible with organic solvents and not stable at higher temperatures. The experiments therefore were limited to mineral oil and ambient temperature conditions.

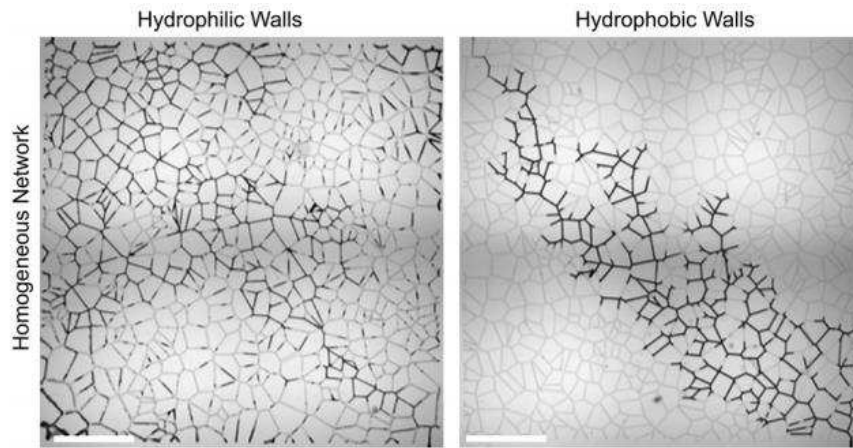


Figure 1.1: Displacement of mineral oil (grey fluid) by water (black fluid) in homogeneous and heterogeneous networks with hydrophilic and hydrophobic walls. (Wu et al. 2012).

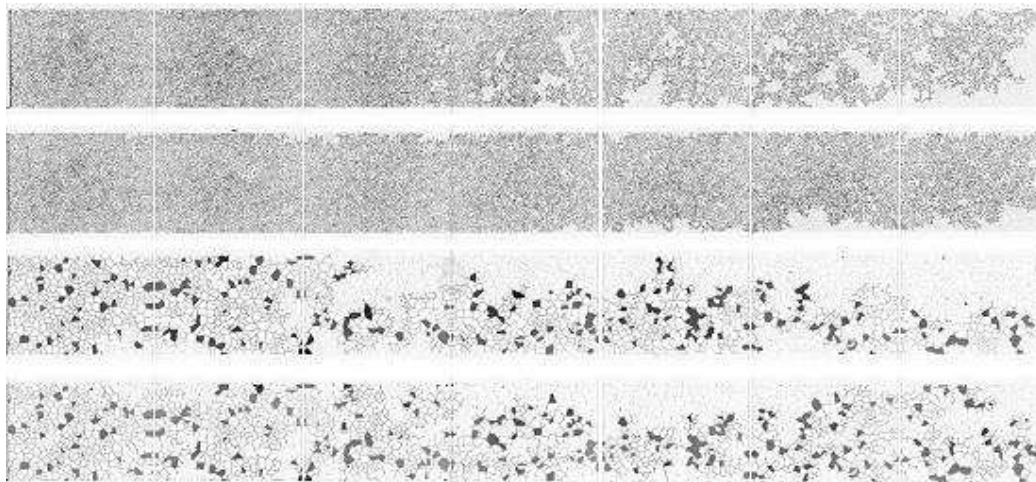


Figure 1.2: Typical brine (NaCl 1.5 wt. %, dyed) saturation patterns in different porous media patterns at breakthrough times (Xu et al. 2014).

Sinton Lab is a University of Toronto based fluidics and energy group who studies different EOR processes using glass micromodels. The group conducted studies on quantitative pore-scale visualization of Steam Assisted Gravity (SAGD) within micromodel pore network (de Haas et al. 2013; Syed et al. 2016). Sinton Lab is also developing microbial enhanced oil recovery (MEOR) and nanoparticle stabilized CO<sub>2</sub> foams (Sinton 2014; Nguyen et al. 2014).

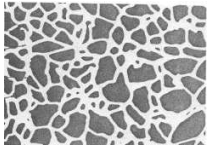
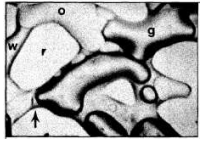

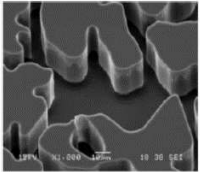
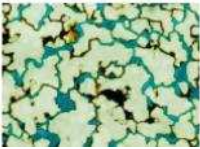
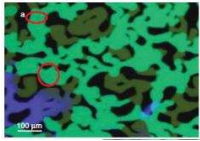


Last, but not the least, a notable work by Howe et al. (2015) used PMMA micromodels to study surfactant EOR phase behavior as a function of salinity and composition of chemicals. There, results from polymethyl-methacrylate (PMMA) micromodels were compared to core plug flooding, where visualization was achieved using NMR core holder. In both micromodel and NMR visualizations, the authors observed similar multiphase flow behaviors, which provided new insights into microemulsion flow and phase formation in porous media.

As reviewed above, there are already many micromodel investigations of various EOR methods (Table 1.1). However, most reviewed studies do not have pore throat dimensions, porosity, and permeability close to those of a real rock. Previous micromodels made at Colorado School of Mines, although specifically made to match pore size, porosity, and permeability of real porous media, were made of materials incompatible with crude oil. In this study, NOA81 micromodels with pore throat dimensions of 10  $\mu\text{m}$  have been made. NOA81 has been widely used in biochemistry micromodel experiments. It is resistant to high temperatures, compatible with organic solvents, and stable for surface treatments (Wagli et al. 2010). High-temperature resistance, along with stability for surface treatments, such as UV-light and plasma bonding, gives an opportunity to use real crude oil, to conduct experiment under reservoir temperatures, and to vary surface wettability in a controllable fashion.

#### **1.4 Organization of the Thesis**

Chapter 1 describes the research objectives and a literature review. Chapter 2 discusses methodology. Chapter 3 presents NOA81 and fluid properties. Chapter 4 presents temperature effect experiments discussion and results. Chapter 5 presents wettability effect experimental results. Chapter 6 presents fractures porous media displacement efficiency experiments. Chapter 7 is research results, conclusions and recommendations.

Table 1.1: List of most cited micromodel studies of petroleum application

Authors	SPE paper#	Width × height of channels in average	Pattern
Danesh et al. 1987	SPE-16956-MS	140-40 μm × 25 μm Not uniform	
Manlowe and Radke 1990	SPE-18069-PA	100 μm × 25 μm Not uniform	
Romero and Kantzas 2007	SPE-89388-PA	30-5 μm × 5 μm, Not uniform	
Buchgraber et al. 2011	SPE-122400-PA	> 80 μm × 25 μm Not uniform	
Farzaneh et al. 2012	SPE-158376-PA	> 100 μm × 60 μm Not uniform	
Shokrlu and Babadagli 2015	SPE-173180-PA	>100 μm × 40 μm Not uniform	
Howe et al. 2015	SPE-174643-MS	200 μm × 60 μm Not uniform	
Bahari et al. 2015	SPE- 171555-PA	200 μm × 60 μm	

## CHAPTER 2

### METHODOLOGY

In this chapter, we present micromodel patterns and fabrication process. Measurements of micromodel properties, such as permeability and hydraulic resistance, are introduced. In the end, we show the experimental setup to visualize multiphase flows, and demonstrate the procedure of phase saturation calculations.

#### **2.1 Micromodel patterns**

Many micromodel studies use periodic geometries or scanned images of rock cross-sections (Gunda et al. 2011; Howe et al. 2015). Neither method, however, can provide controllable porous media properties and at the same time maintain randomness and complexities of a geological porous medium. In this study, as with our previous studies (Xu et al. 2014; He et al. 2015), Voronoi tessellation was used to generate random geometries with controlled porosity and permeability. Voronoi diagrams are widely used in architecture, astrophysics, computational chemistry and material science (Atsuyuki et al. 2000). The algorithm to create porous media based on Voronoi tessellation was first introduced by Wu et al. (2012) and therefore is not repeated here. Figure 2.1 shows the micromodel pattern with a dimension of  $1500\ \mu\text{m} \times 500\ \mu\text{m}$ . This size was determined based on the size requirement of the high-temperature experiments (Chapter 4). Figure 2.2 shows micromodel patterns with a dimension of  $4800\ \mu\text{m} \times 1200\ \mu\text{m}$ . Figure 2.2-A, specifically, is a homogeneous pattern. This pattern will be used in Chapter 5 and 6 to determine the effect of wettability. Figure 2.2-B is a half-fractured pattern designed to study oil recovery in a fractured porous medium without fully penetrating fractures. Figure 2.4-C, on the other hand, is a pattern with fully penetrating fractures. These three patterns are used to study the effect of fractures on the displacement efficiency.

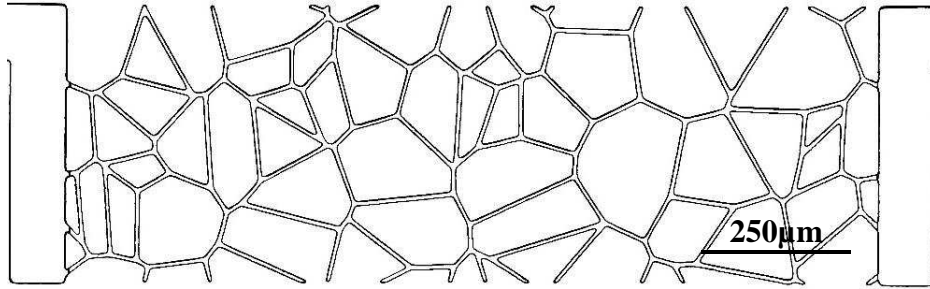


Figure 2.1: 1500  $\mu\text{m}$   $\times$  500  $\mu\text{m}$  micromodel.

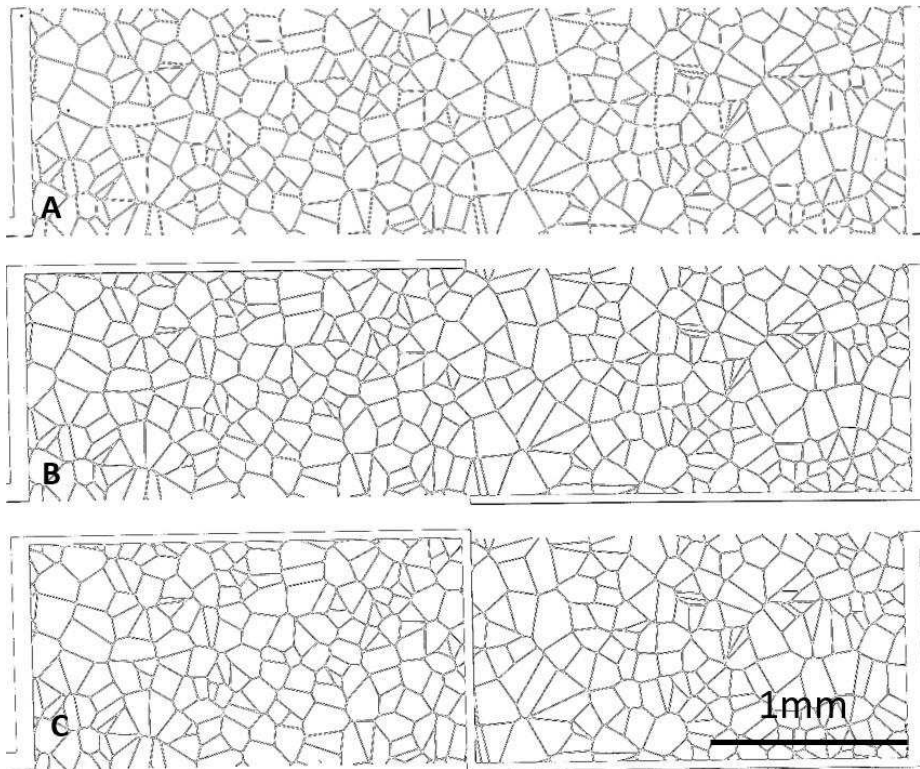


Figure 2.2: 4800  $\mu\text{m}$   $\times$  1200  $\mu\text{m}$  micromodels. A – Homogeneous; B – Half-fractured; C – Fully-fractured pattern.

The size of the channels in these pore geometries were chosen based on properties of typical sandstone formations. In Figure 2.3, Nelson (2009) presented permeability and porosity values for sandstones based on measurements of a thousand wells. In this study, we chose 10  $\mu\text{m}$  channel width and 15% porous medium porosity, which reflect the average values for high-permeability sandstone formations.

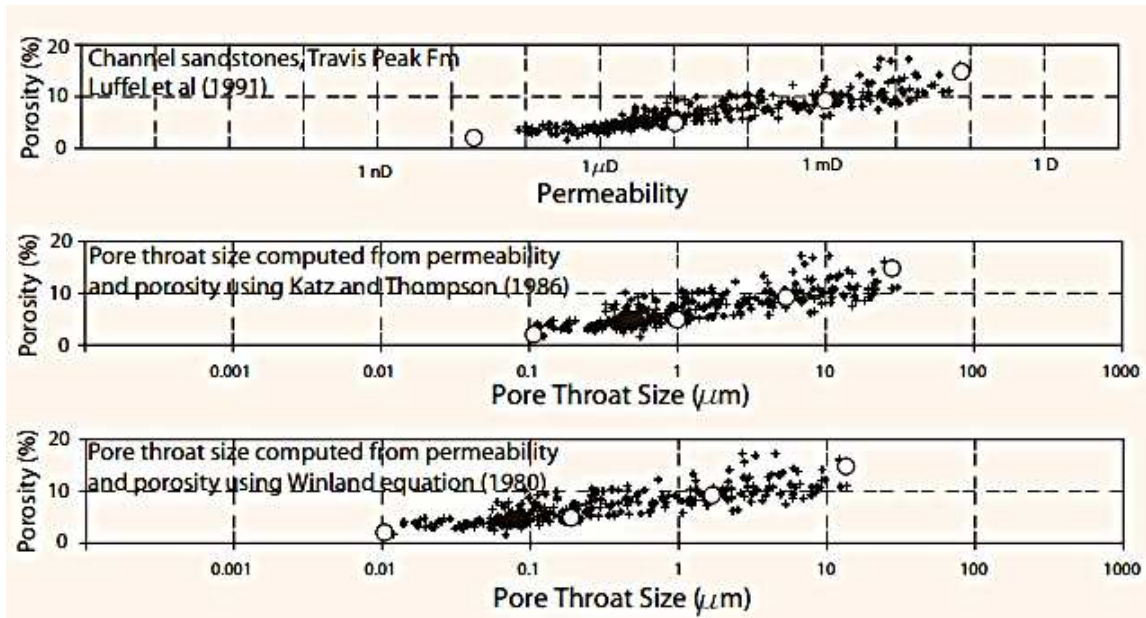


Figure 2.3: Pore throat size, porosity and permeability relationship in sandstones (Nelson 2009).

## 2.2 Fabrication of NOA81 micromodels

Fabrication of NOA81 micromodels starts from porous media pattern design. Patterns as illustrated in Figure 2.1 and 2.2 were converted to CAD files (.dwg), and then printed on photomasks (CAD Services Inc). Photolithography technique was then used to etch the patterns on silicon wafers. The etching procedure is standard and the details may be found in Lin (2009). Two-layer etching was applied to make the porous medium channels 10  $\mu\text{m}$  deep and the inlet / outlet channels 25  $\mu\text{m}$  deep. Figure 2.4 is an SEM image of the inlet channel and the porous medium channels on an NOA81 substrate. The difference in the heights helps to reduce hydraulic resistance before and after the porous medium section, which is essential for accurate absolute permeability measurements and multiphase flow experiments.

Poly(dimethylsiloxane) polymer (PDMS) was used as an intermediate mold to transfer an etched pattern from the silicon wafer to NOA81. PDMS solution was prepared using 10:1 ratio of a base elastomer (184 Sylgard Elastomer) and curing agent (184 Sylgard Curing Agent). Then, PDMS master was molded from the silicon wafer and developed in the oven for four hours at 80°C. After development, PDMS master was peeled off from the silicon wafer.

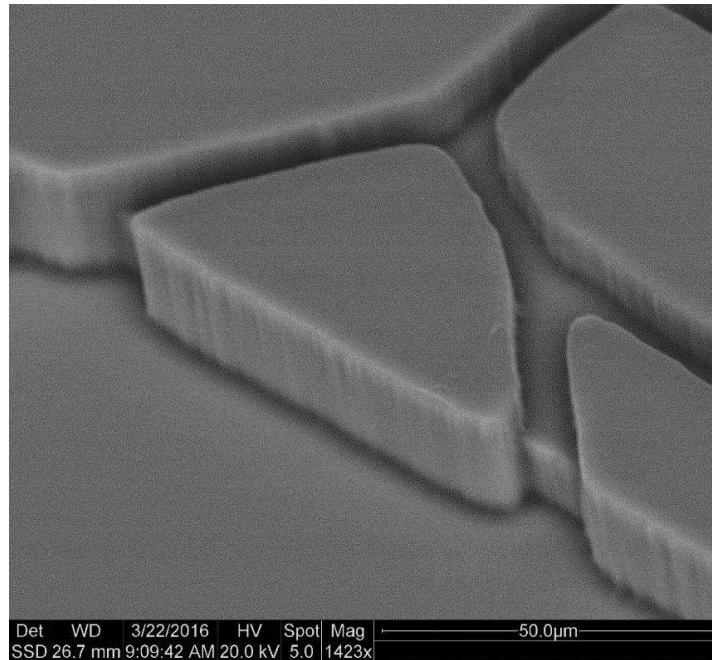


Figure 2.4: SEM image of NOA81 micromodel inlet channel – 60° view.

In many microfluidics studies, oxygen plasma treatment is accepted as a standard bonding method, which works very well in PDMS-to-glass and NOA81-to-glass bonding. Taking into account that glass and NOA81 have different wettability to oil and water, we chose to bond NOA81 and NOA81 surfaces together, as illustrated by in Figure 2.5. An oxygen plasma generates radical oxygen connections on the surface, which creates strong bonds between the two NOA81 surfaces upon contact. However, NOA81 to NOA81 bonding using oxygen plasma was not stable and showed delamination after three hours of exposure to crude oil (Figure 2.6). Despite this issue, modified plasma treatment turned out to be an effective method to modify wettability, and this will be discussed later in Chapter 4.

Due to the delamination issue, another bonding technique, the half-curing method (Levachee et al. 2012), was experimented. This method demonstrates strong NOA81-to-NOA81 bonding in the crude oil environment. In this method, the porous medium pattern is transferred from the PDMS master to NOA81 by UV-light exposure. In the same way, the flat NOA81 substrate is prepared on the glass slide (Figure 2.7).



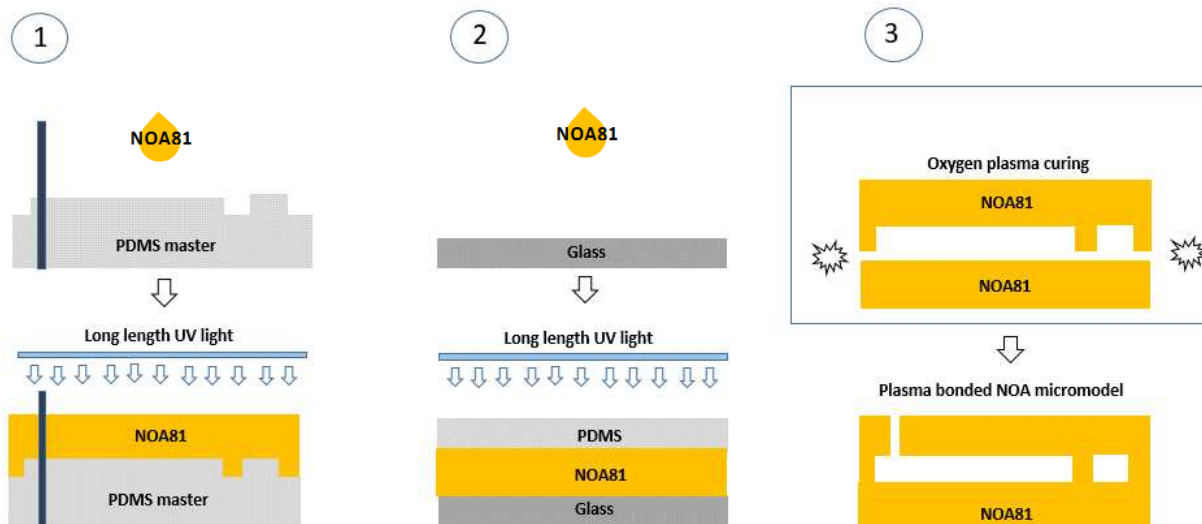


Figure 2.5: NOA81 micromodel fabrication process. NOA81 to NOA81 oxygen plasma bonding method.

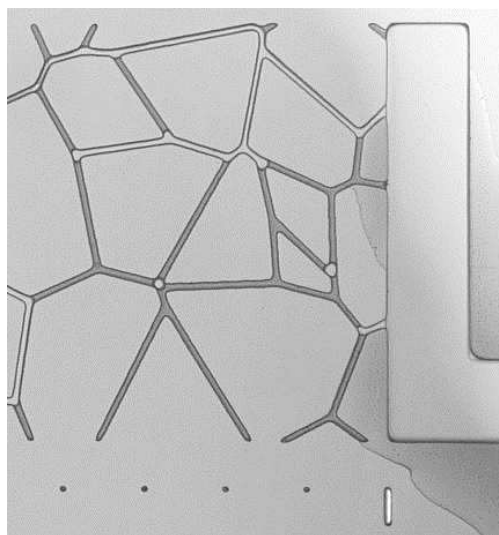


Figure 2.6: Plasma bonding delamination after 3 hours in crude oil environment.

The flat NOA81 substrate is cured only for 40 sec that leaves its surface sticky for further bonding. Then, the patterned NOA81 substrate is pressed gently against the flat NOA81 substrate (Figure 2.7, step 5). Afterwards, UV-light exposure for 60 sec secures the bonding strength (Figure 2.7, step 6). A UVGL-56 (Entela) 365 nm long-wave UV lamp was used to cure NOA81. Then,

Tygon Microbore tubing (ID=0.51mm, OD=1.52 mm) is connected to micromodel and sealed with epoxy glue (Figure 2.7, step 7).

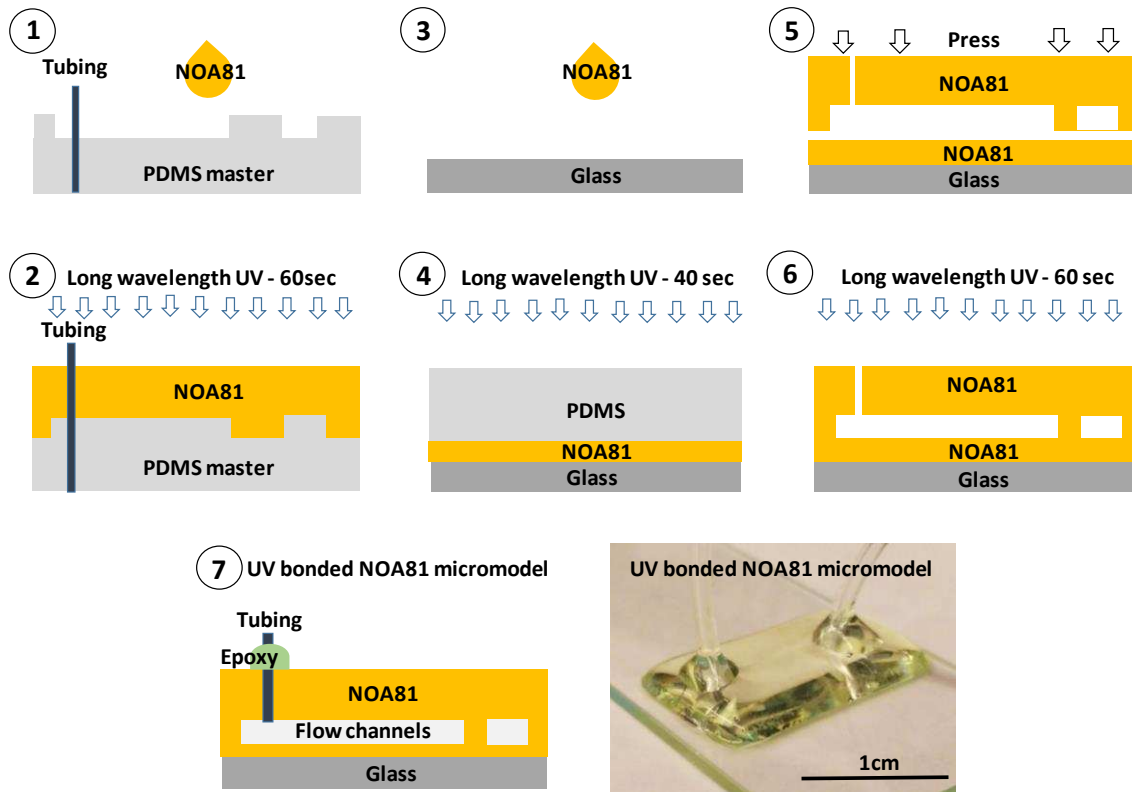


Figure 2.7: NOA81 micromodel fabrication process. NOA81 to NOA81 half-curing bonding method.

After polymerization with long wavelength (365 nm) UV-light for 1 min, a few NOA81 substrates were scanned on profilometer (Tencor Instrument) to verify the dimension of transferred patterns. The scans show 10.6  $\mu\text{m}$  channel depth in the porous medium as opposed to 10  $\mu\text{m}$  designed depth, and 23.5  $\mu\text{m}$  inlet/outlet channel depth as opposed to 25  $\mu\text{m}$  designed depth, with  $\pm 0.5$   $\mu\text{m}$  variation throughout the entire 1500  $\mu\text{m} \times 500$   $\mu\text{m}$  micromodel. The patterns with the dimension of 4800  $\mu\text{m} \times 1200$   $\mu\text{m}$  also had 10.6  $\mu\text{m}$  and 23.5  $\mu\text{m}$  depths for porous medium and inlet/outlet channels, respectively. The channel widths were verified using SEM (Scanning Electron Microscopy) images of NOA81 micromodels. While the channel width in the porous medium was designed to be 10  $\mu\text{m}$ , images of actual samples showed that NOA81 channel width ranges between 8-10  $\mu\text{m}$  (Figure 2.8). This reduction in channel width could be due to the two-

step transfer process, first from silicon wafer to PDMS and then from PDMS to NOA81, or volume reduction of NOA81 during polymerization, which can be up to 3-5% (Hoyle and Bowman 2010).

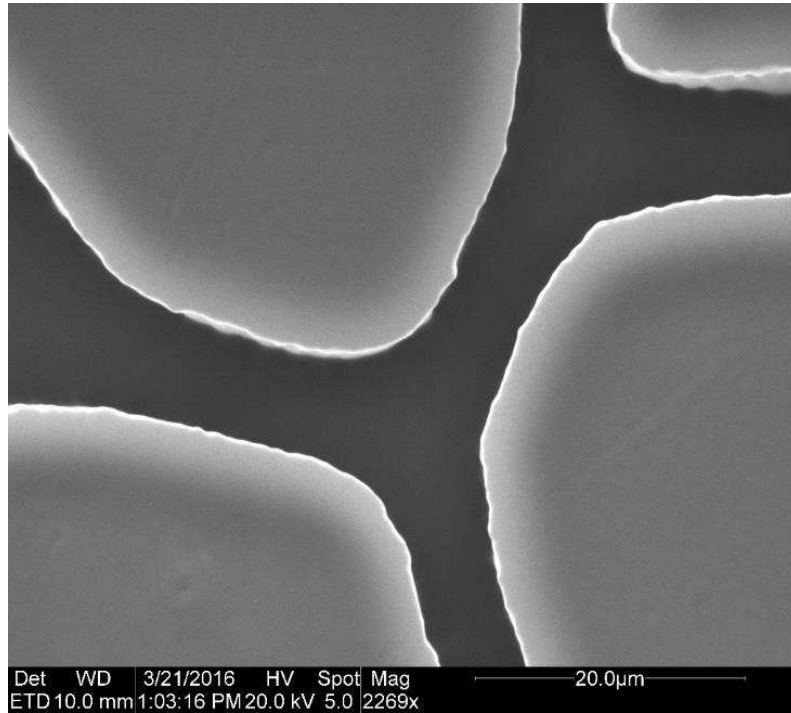


Figure 2.8: SEM image of NOA81 channels in porous medium – top view.

### 2.3 Experimental setup

In this study, a hydrostatic pressure was used to drive fluid flow through micromodels. The hydrostatic pressure of 1.4 psi was created by a 3.3 ft water column in a Tygon tubing (ID 0.508 mm). The pressure at the outlet was the atmospheric pressure. Flow rate was measured by recording the fluid level change over the time in the injection tubing. Figure 2.9 presents the schematics of the experimental setup. This setup is sufficient for single-phase flow experiments that were used to determine permeability of the medium.

For two-phase flow experiments, we used an AmScope600 digital camera to record all two-phase flow experiments. The experiments under reservoir temperature were performed using HCS321 (INSTECH) heating stage, which is connected to MK1000 (INSTECH) temperature controller. Although the heating stage has a built-in temperature transducer, we installed a second temperature transducer to verify the temperature (Figure 2.10).

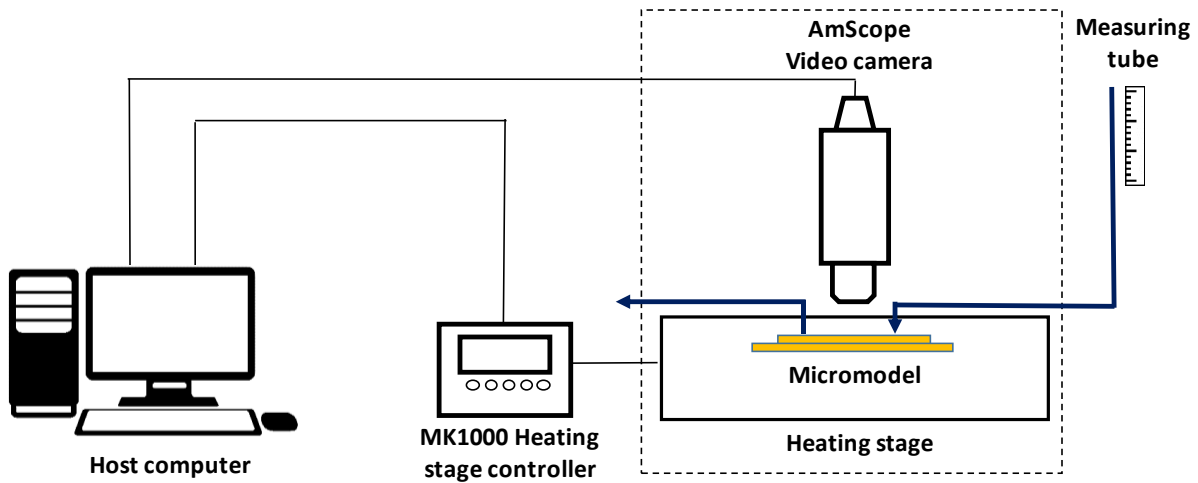


Figure 2.9: Schematic of the experimental setup.

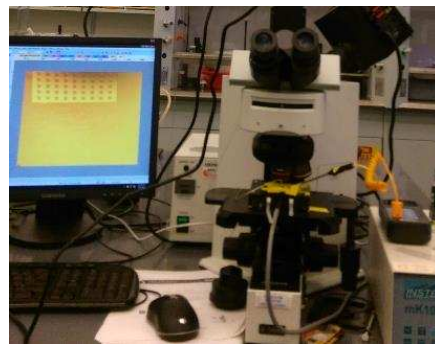


Figure 2.10: Experimental setup.

## 2.4 Micromodel permeability

Permeability of NOA81 micromodels measured from single-phase flow experiments is presented in this section, because permeability is usually treated as a property of “rock”. These single-phase flow experiments use brine (2% KCl) as the saturation fluid. Prior to each experiment, the micromodel was first flooded with the saturation fluid for three hours to eliminate air and trapped air bubbles. As it is difficult to remove air from fractured micromodels, they were placed in the saturation fluid under -0.08 MPA vacuum pressure for 12 hours. NOA81 is impermeable to air, and this is the main reason of prolonged saturation times for NOA81 micromodels.

For permeability measurements, we used a constant pressure difference of 1.4 psi (9987 Pa) to drive the flow. In the experiments, the hydrostatic pressure head decreased at a very slow rate of 9.8 Pa per minute. During a typical experiment, 15 minutes, the change in hydrostatic pressure head is very small and therefore the pressure head can be treated as a constant. Since we know the volume of fluid injected, we can calculate permeability using Darcy's law:

$$Q = \frac{kA \Delta p}{\mu L} \quad (2.1)$$

where  $Q$  is the flow rate through the measuring tube;  $k$  is the permeability;  $A$  is the cross-section area of the micromodel;  $\mu$  is the viscosity of the fluid;  $\Delta P$  is the hydrostatic pressure head;  $L$  is the length of the micromodel.

Flow rate was calculated by:

$$Q = \pi \left(\frac{D}{2}\right)^2 \frac{\Delta l}{\Delta t} \quad (2.2)$$

where  $D$  is the diameter of the measuring tube;  $\Delta l$  is the distance between two marked scales on the measuring tube;  $\Delta t$  is the time interval for the meniscus in the measuring tube to pass a length of  $\Delta l$ .

Substitution of Equation 2.2 into Equation 2.1 gives an equation for the permeability:

$$k = \frac{\mu L \pi \left(\frac{D}{2}\right)^2 \Delta l}{\Delta p w h \Delta t} \quad (2.3)$$

where  $w$  is the width of micromodel;  $h$  is the height of micromodel.

Table 2.1: Porous media pattern permeability

Porous media pattern type	Dimensions, [μm]	Height, [μm]	Porosity	Flow rate [μL/min]	Permeability, [mD]
Homogeneous	1500 × 500	10.6	0.15	0.203	97.23
Homogeneous	4800 × 1200	10.6	0.15	0.137	87.53
Half-fractured	4800 × 1200	10.6 (23.5*)	0.15*	0.27	173.3
Fully-fractured	4800 × 1200	10.6 (23.5*)	0.15*	2.43	1945.68

\* fracture height

\*\* matrix porosity

In permeability calculations, we implicitly assumed that the hydrostatic pressure head and the pressure difference across the porous medium are equal. This assumption holds when the pressure drops in inlet and outlet channels are much smaller than the pressure drop across the porous medium. Here, to verify that this is indeed the case, we calculate the hydraulic resistance of the inlet and outlet channels and compare them to the hydraulic resistance of the porous medium.

Hydraulic resistance of a channel with a rectangular cross-section can be calculated using:

$$R_h = \frac{8\mu L}{r_h^2 A} \quad (2.4)$$

where  $\mu$  is the viscosity of the fluid;  $r_h$  is the hydraulic radius;  $A$  cross sectional area of channel;  $L$  is the length of the inlet / outlet channel.

$$r_h = \frac{2A}{(2w+2h)} \quad (2.5)$$

where  $w$  is the width of a channel;  $h$  is the height of the channel.

Hydraulic resistance of a porous medium, on the other hand, can be calculated from its permeability

$$R_h = \frac{\mu L}{kA} \quad (2.6)$$

where  $L$  is the length of the porous medium,  $k$  is the permeability;  $A$  is the area of the cross-section.

Based on dimensions of inlet and outlet channels and  $k$  of porous media (Table 2.1), hydraulic resistance was calculated. Table 2.2 and Table 2.3 show that the hydraulic resistance of inlet and outlet channels are in general much smaller than the hydraulic resistance of the porous medium. The only exception is the fully -fractured micromodel, whose inlet / out channels' hydraulic resistance is close to 20% of the hydraulic resistance of the porous medium calculated from the permeability. For this porous medium, using Equation 2.3 for its permeability is therefore not accurate. For all the other micromodels, however, the hydrostatic head and the actual pressure drop across the porous medium can be treated as equivalent. The pressure drops before and after the porous medium are indeed negligible.

Table 2.2: 1500  $\mu\text{m}$  x 500  $\mu\text{m}$  micromodel hydraulic resistance

Section	Length, [ $\mu\text{m}$ ]	height, [ $\mu\text{m}$ ]	k, [mD]	$R_h$ , [ $\text{N/s}\cdot\text{m}^5$ ]
Inlet/outlet channel	2000	23.5	-	$1.88 \times 10^{13}$
Porous media	1500	10.6	97.28	$2.95 \times 10^{15}$

Table 2.3: 4800  $\mu\text{m}$  x 1200  $\mu\text{m}$  micromodel hydraulic resistance

Section	Length, [ $\mu\text{m}$ ]	height, [ $\mu\text{m}$ ]	k, [mD]	$R_h$ , [ $\text{N/s}\cdot\text{m}^5$ ]
Inlet/outlet channel	2000	23.5	-	$1.88 \times 10^{13}$
Porous media, homogeneous	4800	10.6	87.53	$1.82 \times 10^{15}$
Porous media, half-fractured	4800	10.6	173.30	$9.19 \times 10^{14}$
Porous media, fully-fractured	4800	10.6	1945.68	$8.13 \times 10^{13}$

## 2.5 Phase saturations

As in Xu et al. (2014), in this study an optical method was used to calculate the saturations of the two phases in micromodel. The saturations were calculated by dividing the pixel counts of each phase by the total pixel count in the pore space. Then, phase saturations were measured at each stage of experiment. The saturation of oil at the point of water breakthrough, specifically, defines the displacement efficiency.

The Olympus 60BX microscope was used to record measurements. The 5X magnification can provide only 1600 $\mu\text{m}$  x 1400 $\mu\text{m}$  observation view, therefore the 4800  $\mu\text{m}$  x 1200  $\mu\text{m}$  micromodels required to take four images to cover entire micromodel area. The first step in image process is thus to stitch the images together using ImageJ-Fiji image processing software. Then, the raw image was sharpened, background subtracted and converted to the binary image. Figure 2.11 shows the sequence of image processing applied to a micromodel saturated with brine solution (2% KCl, DI water, 1% FD&C N1 food dye). All images were taken with identical focus and positional settings, which helps to avoid disturbance to pixel count. Changes in pixel count, therefore, are uniquely correlated to changes in fluid saturations.

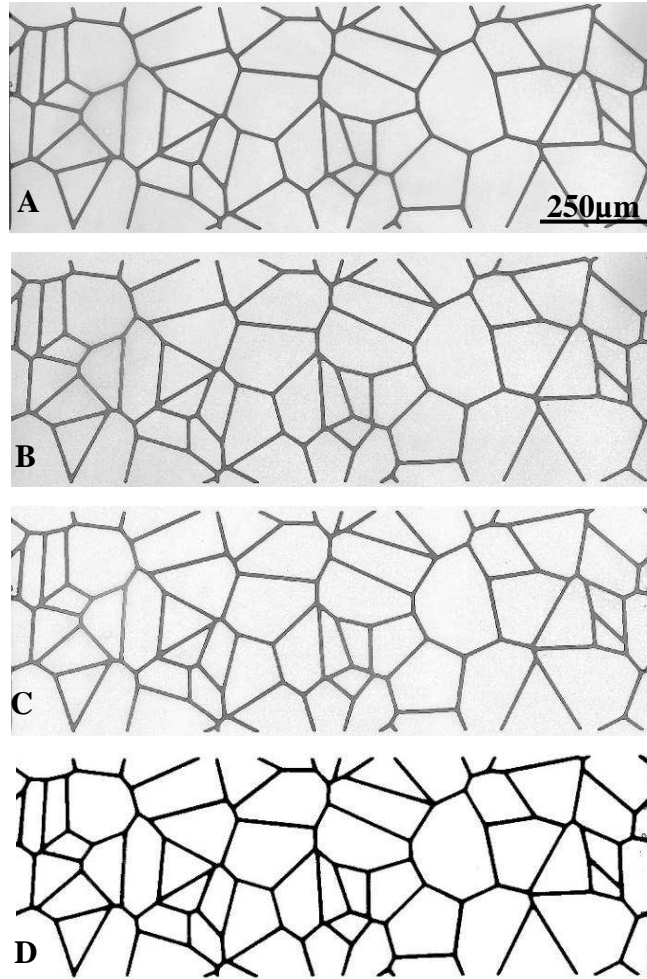


Figure 2.11: Brine saturated micromodel. Image processing steps: A – Raw image; B – Sharpened; C – Background subtracted; D – Converted to binary image.

Note that the pore space after conversion becomes entirely black, the total number of black pixels over the total number of black (255) and white (0) pixels, therefore, gives the porosity of the micromodel (Figure 2.12). Table 2.4 demonstrates saturation calculations based on pixel count. Fully brine saturated taken as a reference image.

After oil saturation, the difference in pixels allows to get irreducible water saturation. In the same way, the difference between initial oil saturation and residual oil saturation is used to calculate the recovery factor by the following equation:

$$RF = \frac{S_w - S_{wi}}{1 - S_w} \quad (2.7)$$



where RF is recovery factor;  $S_w$  is the water saturation;  $S_{wi}$  is the irreducible water saturation.

Figure 2.12 shows phase saturation steps. The first step is to saturate empty micromodel with the brine solution. Then fully brine saturated micromodel is flooded by crude oil to reach irreducible water saturation. Afterward, the micromodel is flooded by brine or surfactant solution to imitate water flooding or surfactant flooding. The difference in pixel count provides water saturation after each stage (Figure 2.12).

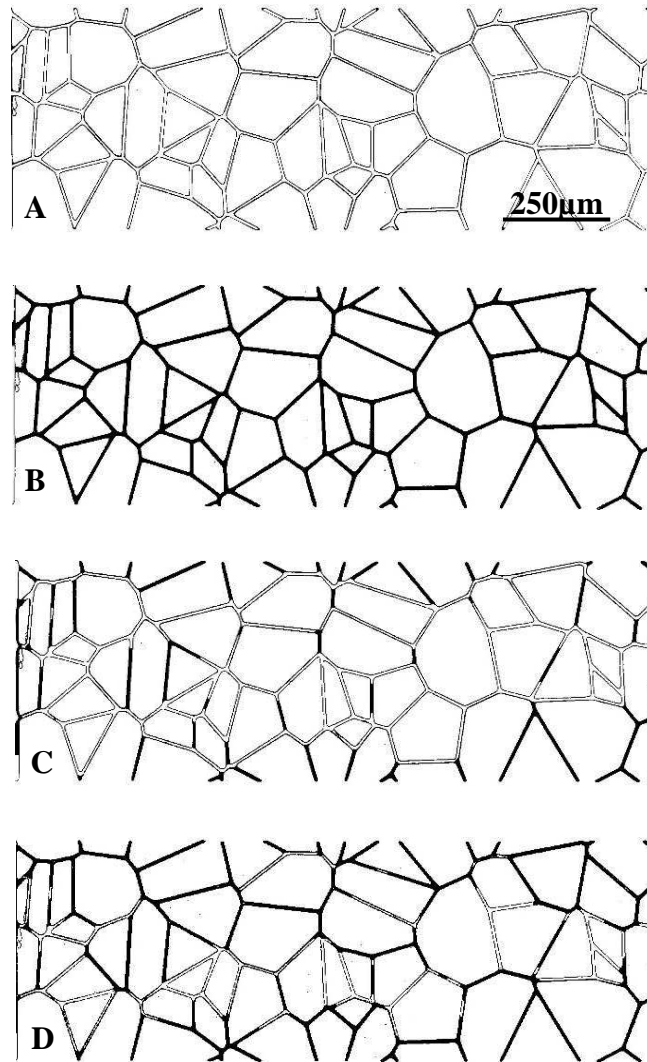


Figure 2.12: Image processing at each experimental step. A – An empty micromodel; B – Water saturation; C – Oil saturation; D - Water/surfactant flooding.

Table 2.4: Phase saturation calculations based on pixel count

Test #	100% water saturation, [pixels]	Irreducible water saturation, [pixels]	Oil Saturation, [pixels]	Water flooding, [pixels]	Residual Oil saturation, [pixels]	Recovery Factor, [%]
1	204065	124798	79267	169189	34876	56%
2	210451	101399	109052	158346	52105	52%
3	209902	131091	78811	173386	36516	53%

## CHAPTER 3

### NOA81 AND FLUID PROPERTIES

#### 3.1 NOA81 Properties

As has been reviewed in the previous chapter, poly(dimethylsiloxane) (PDMS) polymer that was used in the previous studies (Wu et al. 2012; Xu et al. 2014), though being low-cost and easy-to-fabricate, has limitations that it is an elastomer, gas permeable, and not compatible with organic solvents. It swells when contacted with crude oil. To overcome these deficiencies, a primary objective of this study is to use NOA81 (Norland Optical Adhesive, Norland Products Inc.) to fabricate microfluidic micromodels. NOA81 is a single component thiolene resin (Hoyle and Bowman 2010) that polymerizes upon exposure to a long-wavelength (365 nm) UV light. NOA81 is impermeable to air and water (Bartolo et al. 2008), stable on surface treatments (Duffy et al. 1998), has less swelling upon contact with solvents and its elastic modulus is orders of magnitudes higher when compared with PDMS (Wagli et al. 2010).

Norland Products Inc. does not release the composition of the polymer. However, it is accepted that NOA polymer is a mixture of 1,1,1-tris(mercaptomethyl)-propane, trimethylolpropane diallyl ether and isophoronediiisocyanate ester (Figure 3.1). Thiolene bonds (Figure 3.1, between 1 and 2) and thiourethane bonds (Figure 3.1, between 1 and 3) are expected to form upon UV irradiation, while the hydroxyl group in 2 should in principle survive the thiolene reaction and be available for post-functionalization (Silvestrini et al. 2012).

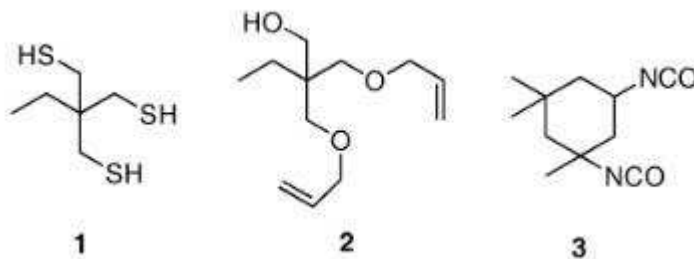


Figure 3.1: NOA81 polymer components (Silvestrini et al. 2012).

## **3.2 NOA81 wettability modification**

Previous work by Xu et al. (2014) used PDMS and glass substrates in micromodel fabrication. As a result, an additional surface treatment step was required to achieve uniform wettability. The authors used oxygen plasma curing to achieve a hydrophilic surface condition and (tridecafluoro-1,1,2,2-tetrahydrooctyl)trichlorosilane vapor deposition to make the inner surfaces of micromodel hydrophobic. Most contact angles in Xu et al. (2014) were measured with air, and only a visual indication of wettability in water-crude oil environment was presented. In this study, as no glass substrate was used, the micromodel has a uniform wettability. Besides, contact angle measurements were conducted in water-crude oil environment using a KRÜSS drop shape analyzer DSA-100. The measurement cell of DSA-100 was first filled with brine (DI water and 2% KCl), and then crude oil was injected to generate a buoyant droplet on the NOA81 surface. The pendant drop method was then used to determine the contact angle of crude oil on the NOA81 surface surrounded by the brine.

NOA81 by nature has both hydrophilic and lipophilic properties (Wagli et al. 2011), which was confirmed in the contact angle measurements. Without any treatment, NOA81 shows an intermediate wettability with a water-oil contact angle of 87°.

### **3.2.1 Water-wet modification**

There are three methods to modify NOA81 surface wettability. The first method is to expose the NOA81 surface to a long-wavelength (365 nm) UV-light for 30 minutes. UV treatment of NOA81 polymer increases surface energy of polymer, which makes the surface more water wet (Levachee et al. 2012). Long time (30 min) UV-light exposure treatment helped to achieve 78° contact angle (Figure 3.2), which is still not strongly water wet.

The second method is based on observations made while conducting oil-water displacements to establish irreducible water saturations in micromodels. It was noticed that NOA81 has a tendency to have preferential wettability to the fluid that it had the first contact. To quantify this observation, we placed NOA81 samples in brine and crude oil for six hours and measured their wettability. The results showed that NOA81 contact angle for brine and crude oil were 81° and 114°, respectively (Figure 3.2).

The third method is to modify wettability by exposing NOA surface to oxygen plasma. Oxygen plasma creates radical oxygen molecules on the NOA81 surface that attract water molecules (Wagli et al. 2010). Oxygen plasma treatment demonstrated excellent water wet characteristics. However, as oxygen plasma bonded micromodels showed delamination after three hours of contact with crude oil, we could not use oxygen plasma bonded micromodels to conduct two-phase flow experiments. To avoid delamination, we combined plasma bonding with the half-curing method. In our combined method, half-cured (40 seconds of curing compared to 60 seconds of complete curing) NOA81 substrates were treated with oxygen plasma, and then bonded together with UV. The bonded micromodel showed no delamination even after 24 hours' of exposure to crude oil environment. Figure 3.3 shows the distribution of dyed brine and oil in an oxygen-plasma-treated micromodel, bonded by the half-curing method, under 20X magnification. The contact angle is clearly hydrophilic, as indicated by the menisci with the pores (Figure 3.3). The contact angle measurements were stable even after 24 hours.

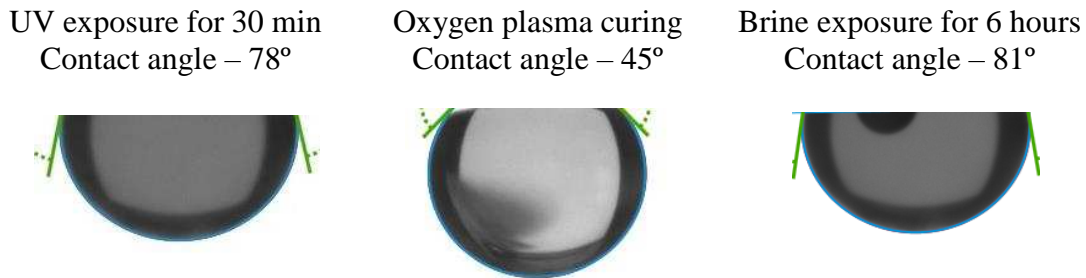


Figure 3.2: Water-wet modification.

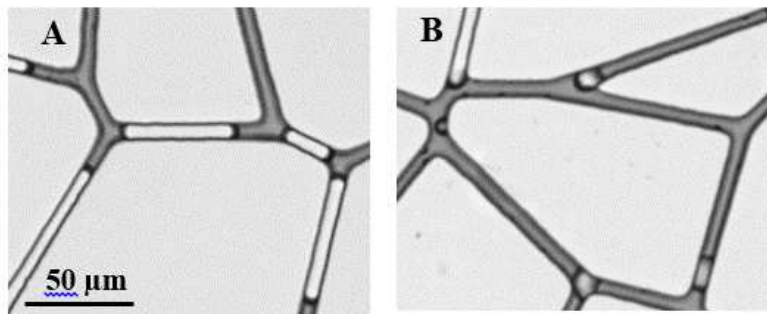


Figure 3.3: 20X magnification of water-wet micromodel. A – Water flooding; B – Surfactant flooding.

### 3.2.2 Oil-wet modification

Cured NOA81 is impermeable to air, and it takes significantly longer time to saturate NOA81 micromodels thoroughly with water or oil compared to PDMS micromodels. Since NOA81 shows preferential wetting to the first liquid that it comes into contact with, increasing exposure time to oil makes NOA81 surface strongly oil wet (Figure 3.4).

Alternatively, an oil wet NOA81 surface can be created by adding APTES ((3-aminopropyl)triethoxysilane) to the uncured (liquid) NOA81 polymer (Silvestrini et al. 2012). APTES wettability modification helped to achieve a contact angle of  $135^\circ$  (Figure 3.4). Also, we tested vapor deposition of (tridecafluoro-1,1,2,2-tetrahydrooctyl)trichlorosilane on NOA81 surface. Although vapor deposition indeed made the surface oil-wet (Figure 3.4), it caused issues in bonding. Therefore, we used APTES to modify NOA81 micromodel wettability to oil wet.

Figure 3.5 shows oil-brine menisci in an APTES-added micromodel at 20X magnification. The micromodel was bonded by the half-curing method. The image shows that the inner surface of the micromodel is highly oil-wet and the contact angle is close to  $135^\circ$  as in Figure 3.5. The measurement results were stable even after 24 hours.



Figure 3.4: Oil-wet modification.

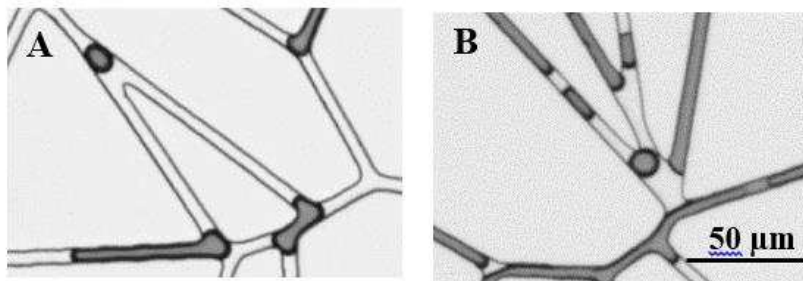


Figure 3.5: 20X magnification of oil-wet micromodel. A – Water flooding; B – Surfactant flooding.

### 3.3 Surface characterization using Fourier transform infrared spectroscopy (FTIR)

Fourier transform infrared spectroscopy (FTIR) was used as an attempt to detect changes in NOA81 surface chemistry after the surface wettability was modified. The IR (infrared) spectroscopy based on irradiation of the molecule by electromagnetic radiation. The molecule bonds have certain frequency of vibration that reflects on absorbance energy. Each molecule bond absorbs energy of a specific frequency, which helps to identify the bond types in an element. Therefore, IR spectrum could be used to determine the functional groups related to the material (Coates 2000). The raw data is processed (OMNIC spectra software) using Fourier Transform to express results in light absorbance for each wavelength form.

NOA81 samples were placed in different environments for six hours and then were analyzed on Nexus 670 FTIR (Thermo Nicolet) equipment. The results were converted to absorbance form, which provides more convenient spectra view (Figure 3.6). The spectra results could be segregated into four regions:  $4000\text{-}2600\text{ cm}^{-1}$ ,  $2600\text{-}2100\text{ cm}^{-1}$ ,  $2100\text{-}1500\text{ cm}^{-1}$  and  $1500\text{-}500\text{ cm}^{-1}$ . In the first region, all NOA81 samples demonstrated three separate wavelength bands except crude oil sample. The absorbance peaks could be related to N-H, C-H and O-H single bonds. In the second region, all samples showed highest peaks that could be related to triple bonds. The third region has connected to previous region band. The peaks could be caused by double bonds such as C=O, C=N and C=C. The crude oil and APTES samples showed the lowest absorbance energy. The last region demonstrated noisy spectra, which could be explained as a large amount of single bonds. The NOA81 FTIR spectrum demonstrated three main absorbance bands, which could be representation of three NOA81 components described in Figure 3.1. However, there is no literature on detailed FTIR analysis of NOA81 available. Therefore, more investigation is needed to explain the wavelength differences between samples exposed to different environments.

The FTIR results may be separated into three groups by the type of environments that the micromodels were exposed to: temperature, surface treatment, and contact fluid. The temperature treatment (Oven cured,  $80^{\circ}\text{C}$ ) shows that there is a notable difference in the absorbance energy and in wavelength peaks. This difference may be related to structural changes of NOA81 since heat is involved in the polymerization process. However, there is no significant difference in wettability between the two samples. In the surface treatment group (oxygen plasma and APTES), the two spectra show similar trends. However, the APTES sample has much lower absorbance energy that resulted in different peak shoulders. The difference in spectra also reflected on

wettability of NOA81 surface: APTES sample is strongly oil-wet and oxygen plasma treated sample is strongly water-wet. In the last group, NOA81 samples exposed to air, brine (2% KCl) and surfactant solution demonstrated almost identical spectra with subtle variation in band shapes, which could explain the common intermediate wettability of all three samples with more water-wet contact angle. The spectrum of the sample exposed to crude oil has very low absorbance energy, which exhibited a completely oil-wet surface.

Overall, the FTIR results showed that the different surface treatments indeed generated differences in the surface chemistry of NOA81, as revealed by the spectra. The higher absorbance resulted in more water-wet surface, in contrary, the lower absorbance gave more oil-wet surface. However, the variations in the spectra cannot be correlated to wettability at this time. A carefully planned study is clearly needed.

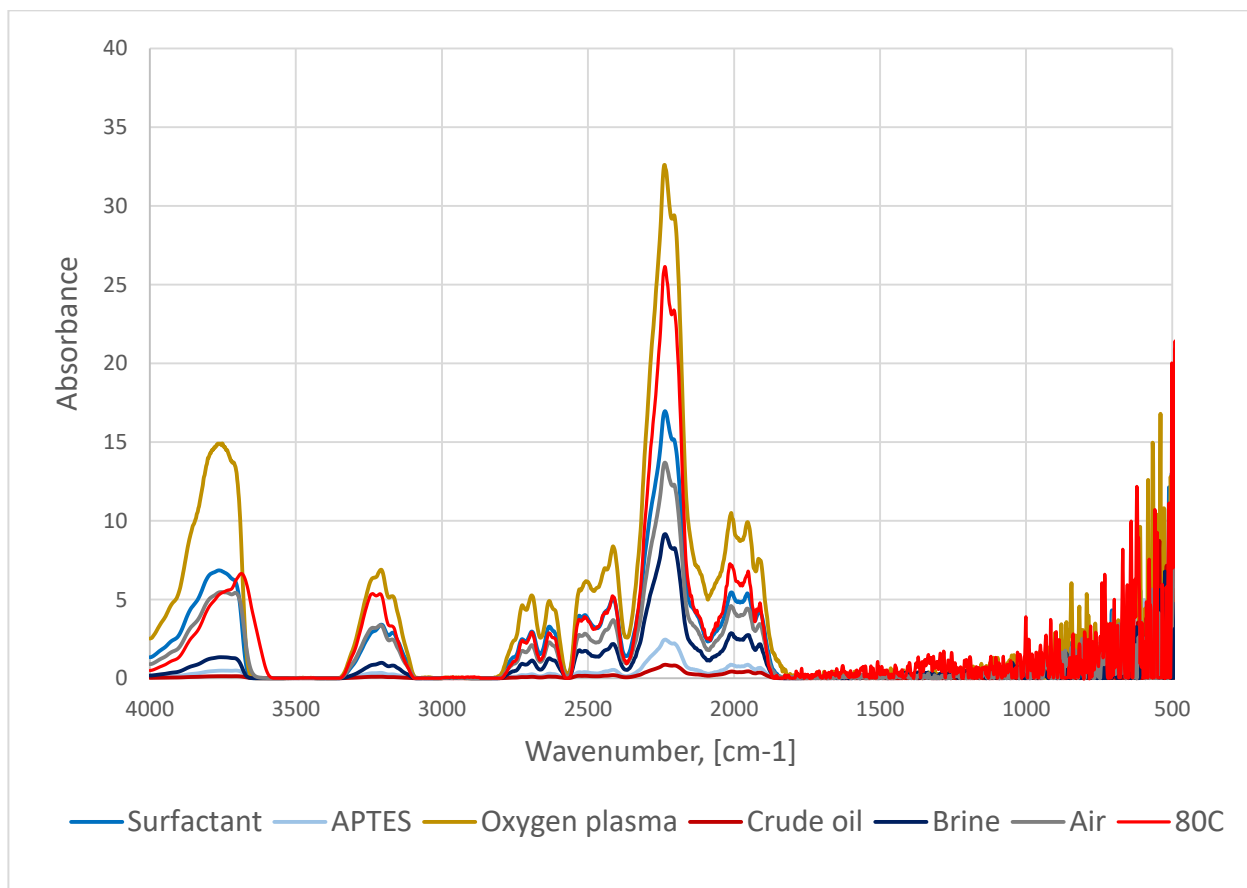


Figure 3.6: NOA81 FTIR analysis.



### 3.4 Fluid properties

In this section, we present the fluids used in the experiments and their properties. In single-phase flow experiments, we used only brine (2% KCL, DI water) to saturate the micromodel and measure the absolute permeability. In two-phase flow (water and surfactant flooding) experiments, brine and a crude oil (38° API) were used. The previous study by Xu et al. (2014) used ethoxylated alcohol as the surfactant, which is non-ionic. Non-ionic surfactants are usually used as co-surfactant, and they are not able to reduce interfacial tension to ultra-low levels. In this study, we used RockOn MX5 (Halliburton) surfactant, which is a mixture of anionic (sulfonate) and non-anionic (ethoxylated alcohol) surfactants. The mixture of anionic and non-anionic surfactants generates a synergy that helps to achieve an ultra-low interfacial tension. In two-phase flow experiments, a food dye (FD&C Blue#1, Spectrum Chemicals) was added to the brine and the surfactant solutions to contrast the fluids in porous media.

#### 3.4.1 Viscosity

Table 3.1 lists the viscosities of the fluids used in the experiments. Viscosity was measured using a capillary viscometer (Cannon-Fenske 50). Measurements of viscosity using capillary viscometers are based on the relation between the kinematic viscosity and the time needed for a given amount of liquid to fall through a capillary tube of a prescribed size. The absolute viscosities of the liquids can be calculated from the kinematic viscosities using the densities of the fluids, measured by a DMA4200M densitometer (Anton Paar Company). The density of fluid is calculated using the frequency of oscillation of a known volume of fluid in a mass-spring system.

Table 3.1: Densities and viscosities of crude oil and water at 20°C and 80°C

Fluid	Density, [g/cm <sup>3</sup> ]	Viscosity at 20°C, [cP]	Viscosity at 80°C, [cP]
Crude oil	0.811	4.525	1.632
Degassed crude oil	0.832	13.73	-
Brine	1.011	0.999	0.383
Surfactant solution	1.015	0.972	0.389

### 3.4.2 Interfacial tension

Interfacial tension (IFT) measurements were conducted using the DSA-100 drop shape analyzer. The crude oil was injected into brine/surfactant solution through a capillary, and IFT was calculated based on the equilibrium shape of the drop impinging on the tip of the capillary. Figure 3.7 presents equilibrium shapes, IFT obtained at ambient and reservoir temperatures. The increase in the temperature from 20°C to 80°C reduced IFT from 23.3 mN/m to 18.41 mN/m. At 20°C, surfactant reduced IFT by one order of magnitude. At 80°C, IFT was further reduced. DSA-100 generated a result of 0.61 mN/m but such low IFT cannot be reliably measured using DSA-100. Therefore, the measurements need to be repeated on spinning drop tensiometer.

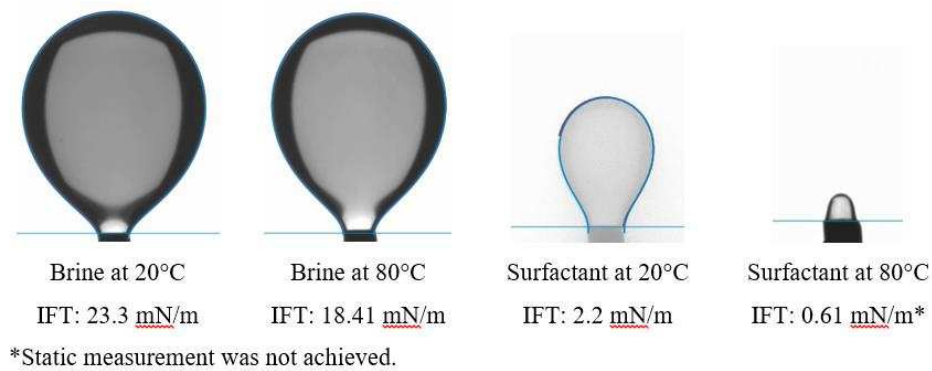


Figure 3.7: IFT measurement results

## CHAPTER 4

### EFFECT OF TEMPERATURE

In this chapter, we compare water flooding and surfactant flooding at ambient (20°C) and reservoir (80°C) temperatures using the 1500  $\mu\text{m} \times 500 \mu\text{m}$  micromodel, whose dimension was designed to fit into the heating stage. The micromodel did not undergo any surface treatment, therefore had an intermediate wettability.

The micromodel was first saturated with a brine solution (2% KCl). Then, the crude oil was injected until the irreducible water saturation was reached, which was typically 8%. Generally, elevated temperature helps to reduce saturation time. The next step was injection of the displacing fluid to simulate water or surfactant flooding. The pressure difference created by one meter of water column, 9978 Pa or 1.4 psi, generates a flow rate of 0.2  $\mu\text{L}/\text{min}$  in single-phase (brine) flow. The micromodel has very small pore volume, 0.0012  $\mu\text{L}$ . The recovery as a function of pore volume (PV) injected will therefore be presented using logarithmic scale.

#### **4.1 Displacement efficiency at the ambient temperature 20°C**

Figure 4.1 (A, B) compares the distributions of water and oil phases of a typical water flooding and a typical surfactant flooding. In water flooding, crude oil was trapped mostly in channels perpendicular to the flow direction and in dead-end pores of the porous medium. Channels have different flow velocities, because they have different lengths and angles relative to the flow direction. When several channels meet at an intersection point, oils in slow-moving channels are snapped off, leaving behind the residual oil saturation. The overall displacement is therefore not a uniform piston-like movement. In contrast, surfactant flooding was able to displace most of the trapped oil even in channels that are perpendicular to the mean flow direction. However, it was noticed that the channels with irreducible water saturation resisted the displacement (Figure 4.1). We believe that it took place due to Jamin effect, which refers to a capillary resistance to flow when two phases are present in the same channel (Green and Willhite 1988).

The breakthrough took place within a second after the displacing fluid enters the porous medium. However, in some experiments, it took up to five seconds to breakthrough. The reason for a longer breakthrough time could be different relative permeability for the individual experiment. It was observed that after the breakthrough, there was no significant additional oil

recovery even after injecting 1000 PV. Figure 4.2 shows the recovery factor as a function of pore volume injected. Each data point is an average of three experiments. Water flooding recovery factor at breakthrough was 53%, and it did not change significantly with additional injection. The recovery factor only improved by 2% at 100 PV. In contrast, surfactant flooding recovered 66% of oil at breakthrough. At 100 PV, additional 12% oil was recovered. The difference in the recovery factors between water flooding and surfactant flooding is well explained by the almost tenfold IFT reduction, from 23.3 mN/m to 2.2 mN/m, created by the surfactant (Figure 4.5).

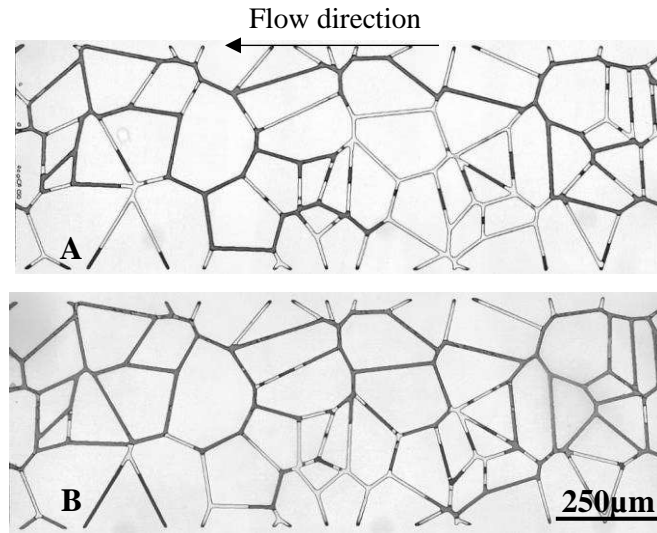


Figure 4.1: Distributions of oil and water phases at breakthrough. A –water flooding at breakthrough. B – surfactant flooding at breakthrough.

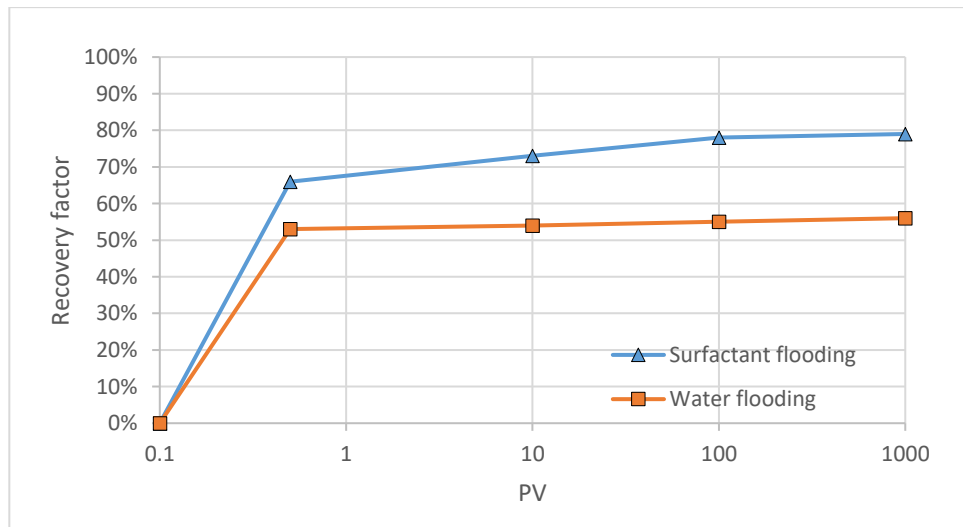


Figure 4.2: Displacement efficiency at ambient temperature.

## 4.2 Displacement efficiency at a high temperature 80°C

Figure 4.3 shows the distributions of oil and water phases in water flooding and surfactant flooding at 80°C. Here, oil was trapped by the same mechanisms as at 20°C. However, it was noticed that elevated temperature reduced the irreducible water saturation in both dead-end pores and connected channels. Oil saturation phase took 30 minutes, which was six times quicker than at ambient temperature. Besides, the irreducible water, brine solution, appeared to be more concentrated in color at 80°C. Increase in dye concentration could take place due to losing the aqueous part of dyed brine solution. After flooding, it is apparent that surfactant has again effectively reduced oil saturation in the porous medium.

In Figure 4.4, oil recoveries of water flooding and surfactant flooding at 80°C are presented as functions of pore volume injected. Despite of the almost identical mobility ratio, the displacement efficiency of water flooding at 80°C was lower than that at 20°C. At breakthrough, the displacement efficiency of water flooding was 44%. After breakthrough, only 2% of additional oil recovery was achieved with 100 PV injection, same as the additional recovery achieved at 20°C at 100 PV. In surfactant flooding, oil recovery at breakthrough was 68%, which was slightly higher than that at 20°C. With continuing injection of surfactant solution, the recovery factor was increased to 11%.

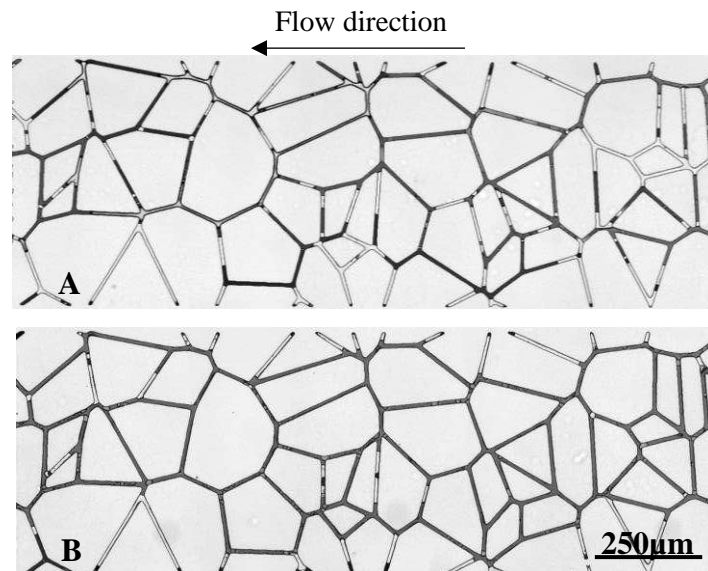


Figure 4.3: Reservoir temperature displacement efficiency. A – Water flooding at breakthrough. B – Surfactant flooding at breakthrough.

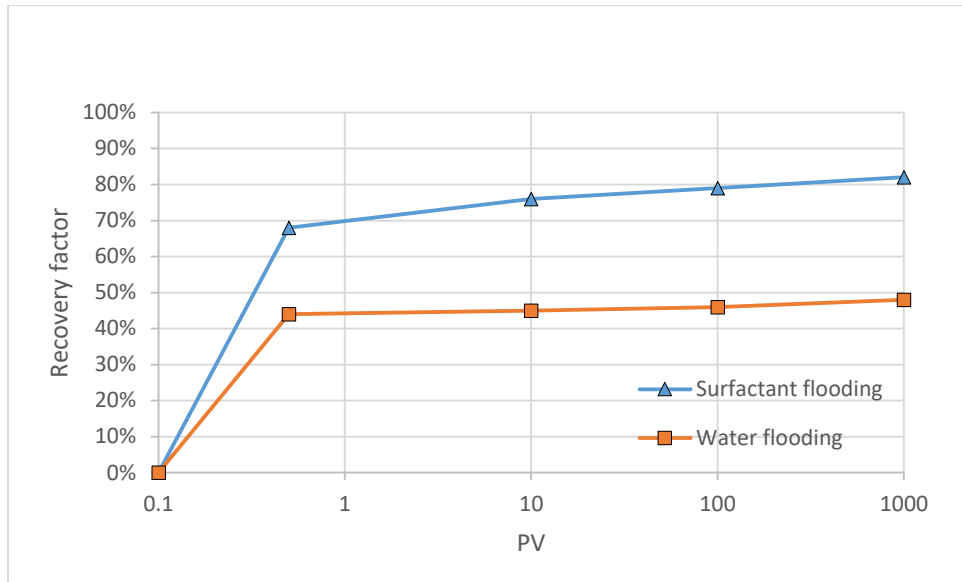


Figure 4.4: Oil recoveries at 80°C as functions of PV injected.

### 4.3 Correlating displacement efficiency to capillary number

Capillary number is an important dimensionless number that controls the dynamics of multiphase displacement in a porous medium. In this Chapter, as viscosity ratio is nearly independent of temperature, capillary number is the only dimensionless parameter that saw significant changes with temperature. Table 4.1 shows that capillary number increases with decreasing IFT. As IFT decreases with increasing temperature and viscosity decreases with increasing temperature, capillary number in the table increases with increasing temperature. In Figure 4.5, recovery factors at breakthrough are plotted against capillary number, and a reasonable correlation may be observed. Whenever the capillary number was increased by an order of magnitude, recovery factor improves significantly. In water flooding, the IFT reduction of 22% from temperature increase did not change oil recovery dramatically, even reduced recovery factor for 7%. The reason for lower recovery could be reduction of irreducible water saturation caused by injection fluid, the phenomena observed in high temperature oil saturation (Figure 4.6). In surfactant flooding, increasing temperature reduced IFT from 2.2 mN/m to 0.6 mN/m, which helped to increase the magnitude of the capillary number by one order of magnitude.

Table 4.1: Capillary number

Process	IFT, [mN/m]	$N_c$
Water flooding 20°C	23.3	$2.9 \times 10^{-5}$
Water flooding 80°C	18.4	$3.7 \times 10^{-5}$
Surfactant flooding 20°C	2.2	$3.1 \times 10^{-4}$
Surfactant flooding 80°C	0.6*	$1.1 \times 10^{-3}$

\* Static measurement was not achieved.

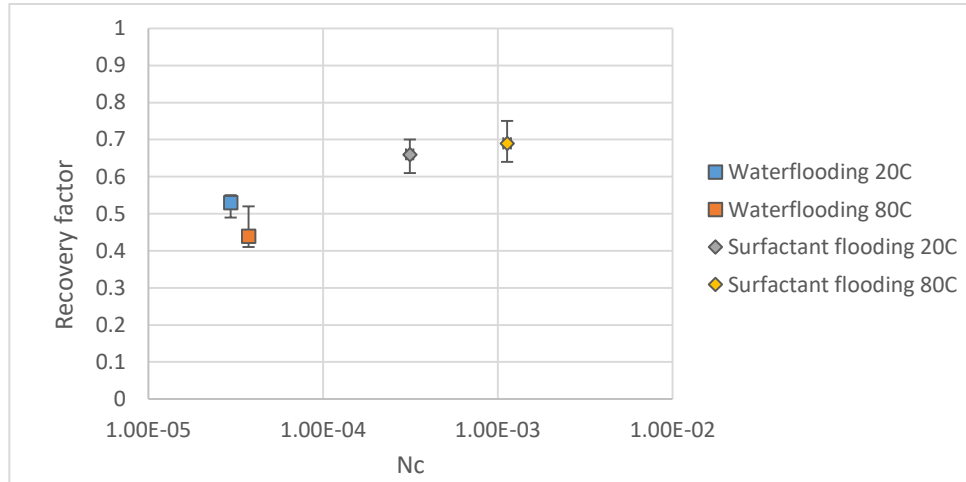


Figure 4.5: Oil recovery factor at breakthrough plotted against the capillary numbers.

#### 4.4 Interesting observations

As we conducted these experiments, we observed several interesting phenomena. These phenomena are described below in this section.

##### 4.4.1 Oil-water replacement in dead-end pores

As we used oil to displace brine to establish the irreducible water saturation, an interesting phenomenon was observed in dead-end pores, that brine in dead-end pores was slowly replaced by crude oil. Here, we use “replace” instead of “displace” to emphasize that brine in dead-end pores is not removed by displacement. Figure 4.6 is a sequence of images that demonstrate the “replacement” process. The flow direction of the oil is from top to bottom. Time step images show clearly that in a Y-type dead-end pore, brine in both channels was slowly replaced by oil, and one of the channels has a higher rate of replacement than another. As brine and oil are immiscible, this

observation suggests that brine may have left the dead ends along the walls and corners of the channels. Although there is no direct evidence of flow along walls and in the corners due to the limitation in the magnification of the optics, it was indeed observed that there is fluid drag force along micromodel, and this may be due to brine present along the walls and in the corners. For brine that resides along the walls and corners, shearing may act as a mechanism that slowly removes the brine from the dead ends. The presence of strong shear in trapped fluid pockets is evidenced in Figure 4.7. In a crude oil pocket left behind the displacement front in an inlet channel, a small particle was found to rotate, caused by the shear that comes from the movement of the brine nearby.

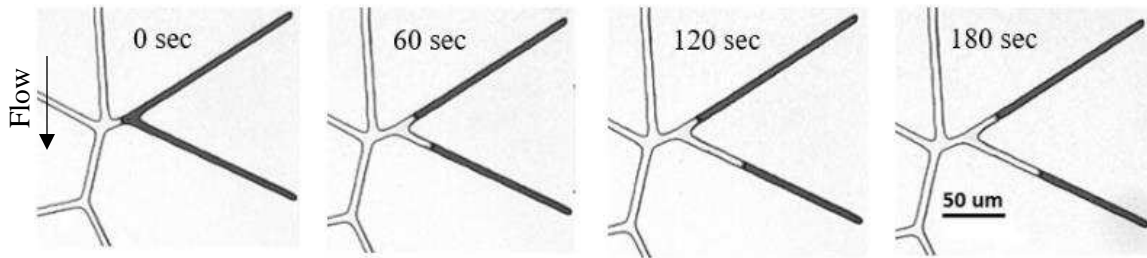


Figure 4.6: Dead-end pore displacement at each 60 second time frame.

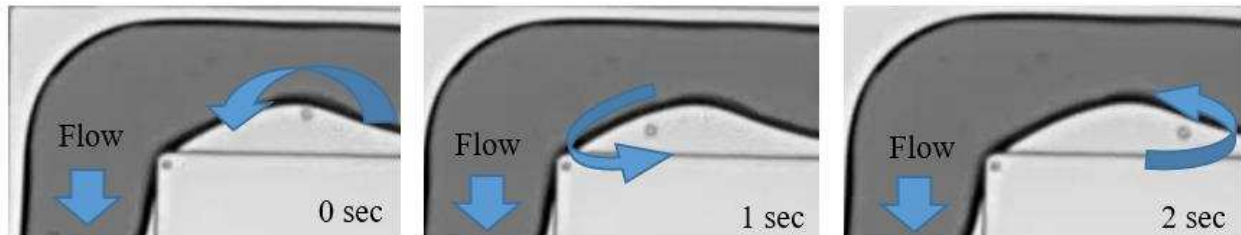


Figure 4.7: The particle rotational movement in inlet channel.

As the dimension of the inlet channel ( $100\ \mu\text{m}$ ) is much larger than the dimension of the channels in the micromodel, flow velocity within the micromodel should be higher than that in the inlet channel due to reduced flow cross-sectional area in porous media. Therefore, shear-induced flow could be responsible for the replacement of brine with oil in dead-end pores.



#### 4.4.2 Microemulsion

In surfactant flooding experiments, formation of microemulsion was observed. Figure 4.8 is a magnified view (20X) of the microemulsion droplets. Figure 4.8 demonstrates the difference between surfactant flooding and water flooding regarding microemulsion generation in porous media. The experiments were conducted at 20 °C. Droplet size in the microemulsion varied from 1  $\mu\text{m}$  to 25  $\mu\text{m}$ . Apparently, these are oil droplets surrounded by the surfactant solution. Whether the type, quality and stability of the emulsion is the same as those formed in test tubes is an interesting question that can be further studied.

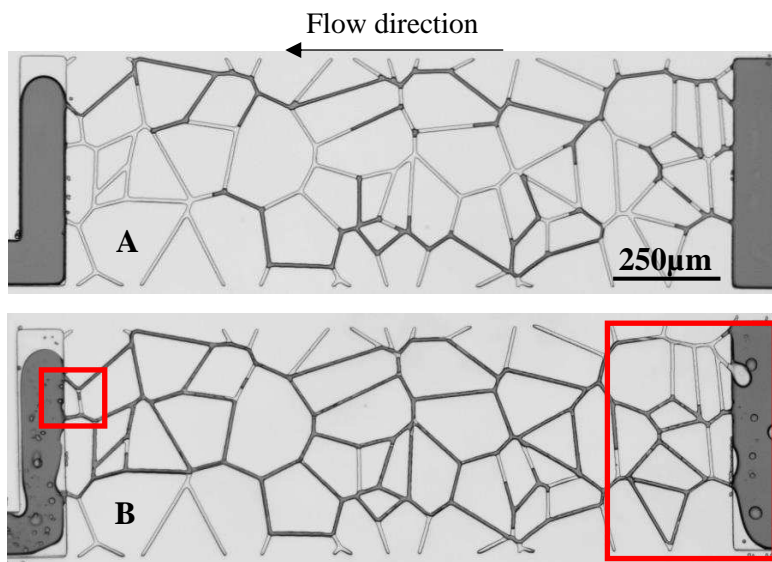


Figure 4.8: Water-oil displacement patterns at 100 PV. A – Water flooding. B – Surfactant flooding. Microemulsions in the inlet and outlet channels are highlighted.

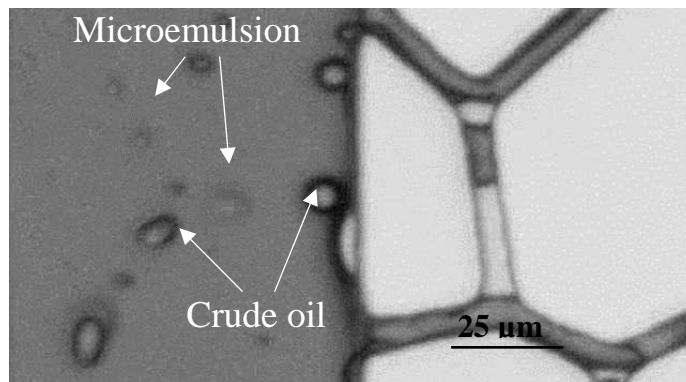


Figure 4.9: A magnified view (20X) of microemulsion in the outlet channel.

### 4.4.3 Flow reversal in a network of pores

In a network of pores, owing to wettability and differences in pore size, flow reversal, which is a phenomenon that the displaced fluid moves upstream of the imposed mean flow, could take place. Even though our micromodel contains nearly identical pores and the wettability is nearly neutral, we still observed a few instances of flow reversal in surfactant flooding at 20°C. An example of reversed flow is presented in Figure 2.10, where it can be clearly seen that an oil droplet, owing to the reversed flow, was produced into the inlet channel.

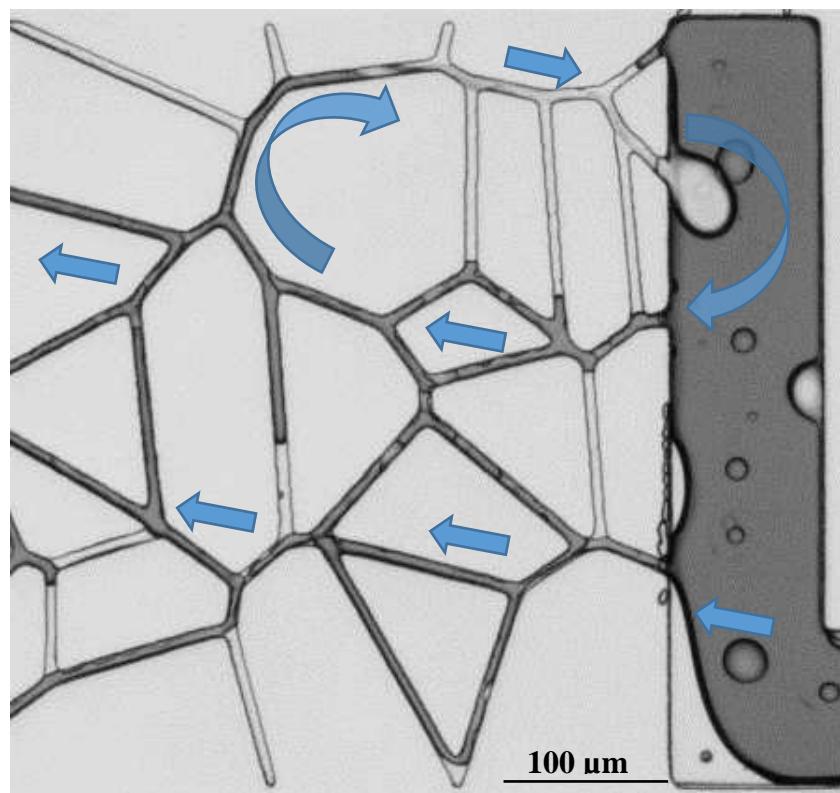


Figure 4.10: Reversed flow observed at the interface between the inlet channel and the porous medium micromodel.

### 4.5 Summary

In this chapter, we conducted water flooding and surfactant flooding at 20°C and 80°C to study the temperature effect on recovery factor. Results from this chapter show that the change in IFT is the primary factor controlling oil recovery. At 20 °C, surfactant flooding achieved 66% oil recovery at breakthrough, 15% higher than water flooding. At 80 °C, surfactant flooding increased

recovery from 44% to 68%. In water flooding, after breakthrough, there was no significant oil recovery. In contrast, surfactant flooding achieved 15% and 22% additional oil recoveries with additional injection, for 20 °C and 80 °C, respectively. Oil recovery at breakthrough can be well correlated to the capillary number, the dimensionless number that controls the displacement process. Several interesting phenomena were observed: replacement of fluid in dead-end pores, generation of microemulsion, and reversed flow. Closer investigation of these phenomena could give new and additional insights into the dynamics of multiphase flow in porous media.

## CHAPTER 5

### EFFECT OF WETTABILITY

This chapter examines water flooding and surfactant flooding in micromodels of different surface properties. In addition, two kinds of oil were used, including a degassed crude oil to illustrate the effect of mobility ratio. Degassed oil was achieved by placing crude oil in -0.08 MPa vacuum for 12 hours. Viscosity ratio of crude oil to degassed crude oil is one to three.

In these experiments, we used a different approach to establish the initial oil saturations. In the previous chapter, the initial oil saturation was established by a pressure driven flow of oil into a brine-saturated micromodel. That method not only takes a long time, it is also not compatible with methods to control surface wettability, as endured contact with crude oil weakens the strong water-wet properties of NOA81. In this chapter, an HA70-3007 (Harvard Apparatus) syringe pump was used to saturate micromodels with crude oil. The saturation time was significantly reduced from six hours to ten minutes because of the high-flow-rate (10 $\mu$ L/min) injection.

Compared with crude oil, degassed oil has different IFT with brine and surfactant solution. Table 5.1 presents the IFT for degassed oil, and the corresponding capillary numbers for water flooding and surfactant flooding. The capillary numbers of flooding presented in the previous chapter are also included for comparison.

Table 5.1: IFT and capillary number

	IFT	$N_c$
Water flooding	23.3	$7.6 \times 10^{-06}$
Surfactant flooding	2.2	$8.1 \times 10^{-05}$
Water flooding of degassed oil	26.6	$6.7 \times 10^{-06}$
Surfactant flooding of degassed oil	3.3	$5.4 \times 10^{-05}$

#### 5.1 Displacement in water-wet micromodels

Figure 5.1 shows the distribution of brine and oil in water flooding in a water-wet micromodel. The distribution was recorded at 10 PV. The distribution was uniform due to imbibition. Breakthrough took place in 10 seconds, and the recovery factor was 73%. After breakthrough, there was only 2% of additional oil recovery, measured at 10 PV. Figure 5.2 shows surfactant flooding in water-wet micromodel at 10 PV. Although, the breakthrough time of surfactant

flooding was the same as that of water flooding, the recovery at breakthrough was 80%, and continuing injection led to 13% of additional recovery at 10 PV (Figure 5.2).

Then, the experiments were repeated with degassed crude oil to test the effect of an unfavorable mobility ratio. Figure 5.3 and Figure 5.4 show the distributions of phases at 10 PV, for water and surfactant floodings, respectively. From pixel counting, it is found that the unfavorable mobility ratio introduced by the use of degassed oil reduced water flooding recovery to 65% at breakthrough, 8% less than crude oil. Only 1% additional recovery was measured at 10 PV. In surfactant flooding, the recovery factor was 60%, 20% less than in lower viscosity oil and, surprisingly, 5% lower than water flooding. With additional injection, however, 15% additional recovery was achieved at 10 PV.

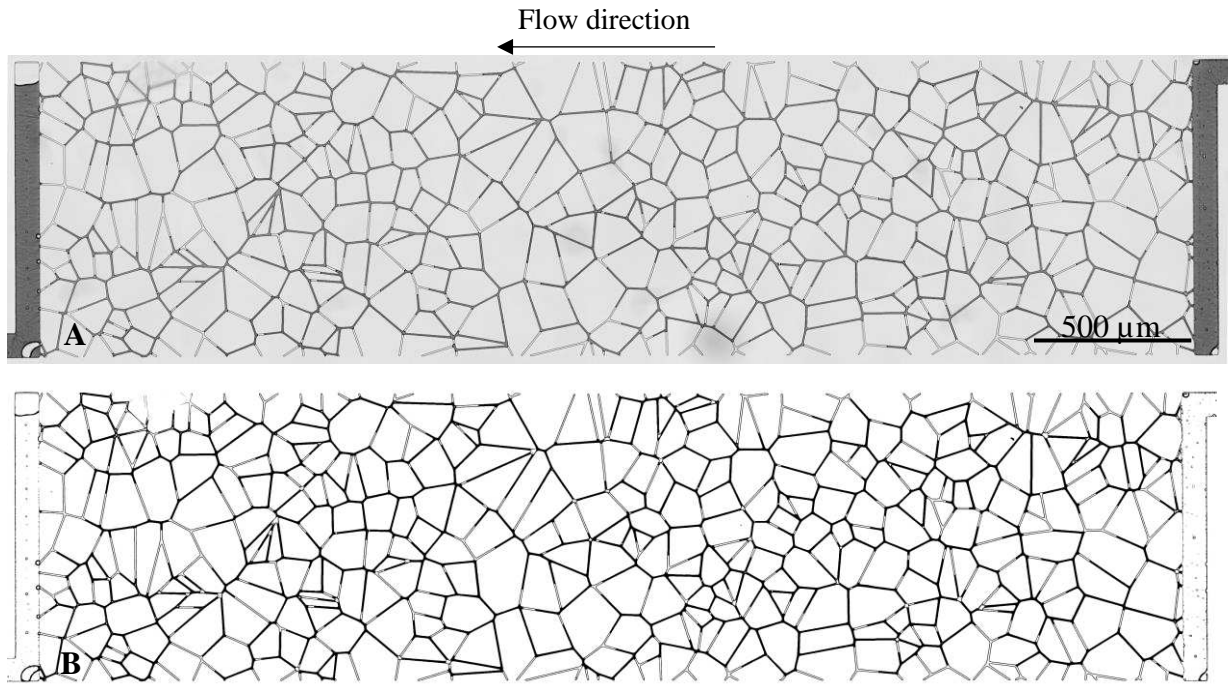


Figure 5.1: Water flooding in water-wet micromodel at 10 PV. A – Raw image; B – Binary image.

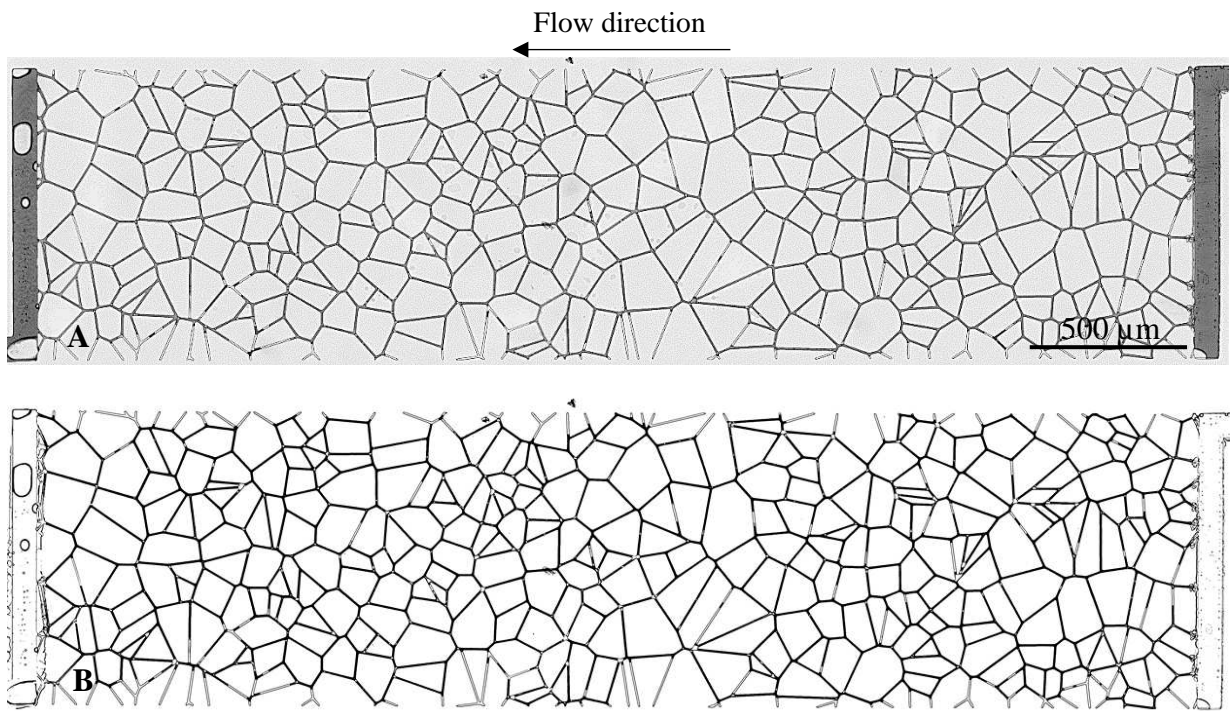


Figure 5.2: Surfactant flooding in water-wet micromodel at 10 PV.  
A – Raw image; B – Binary image.

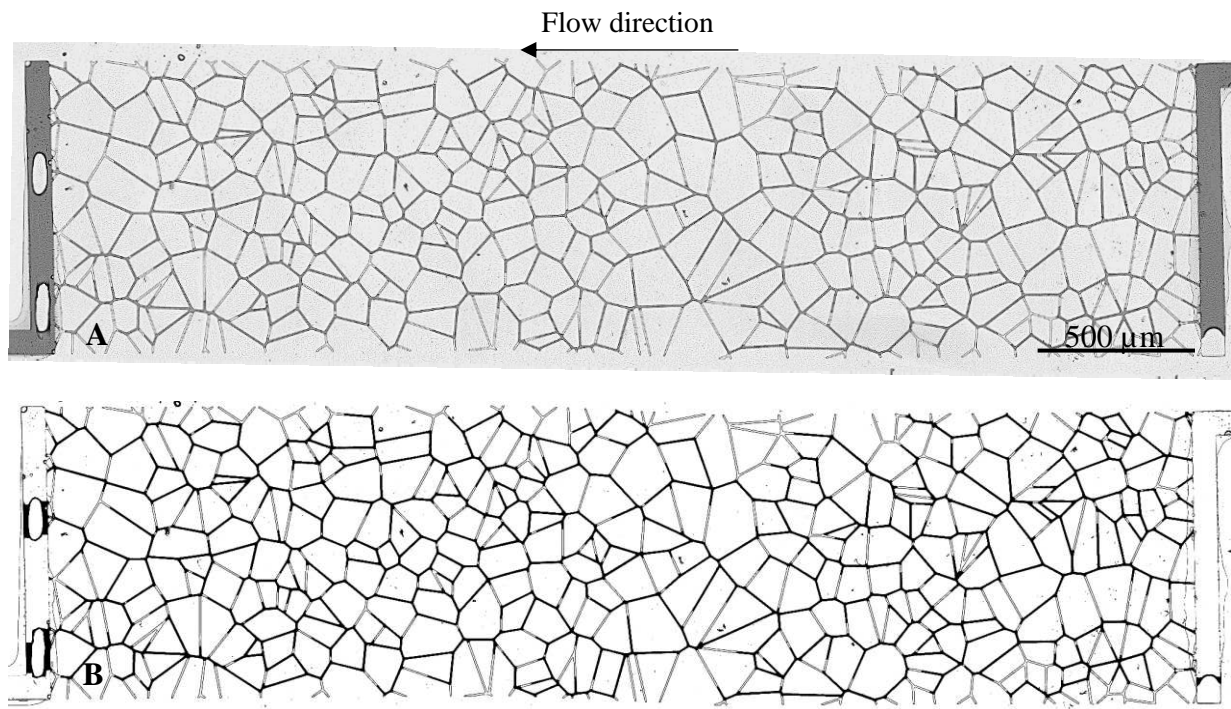


Figure 5.3: Water flooding in water-wet micromodel with degassed crude oil at 10 PV.  
A – Raw image; B – Binary image.

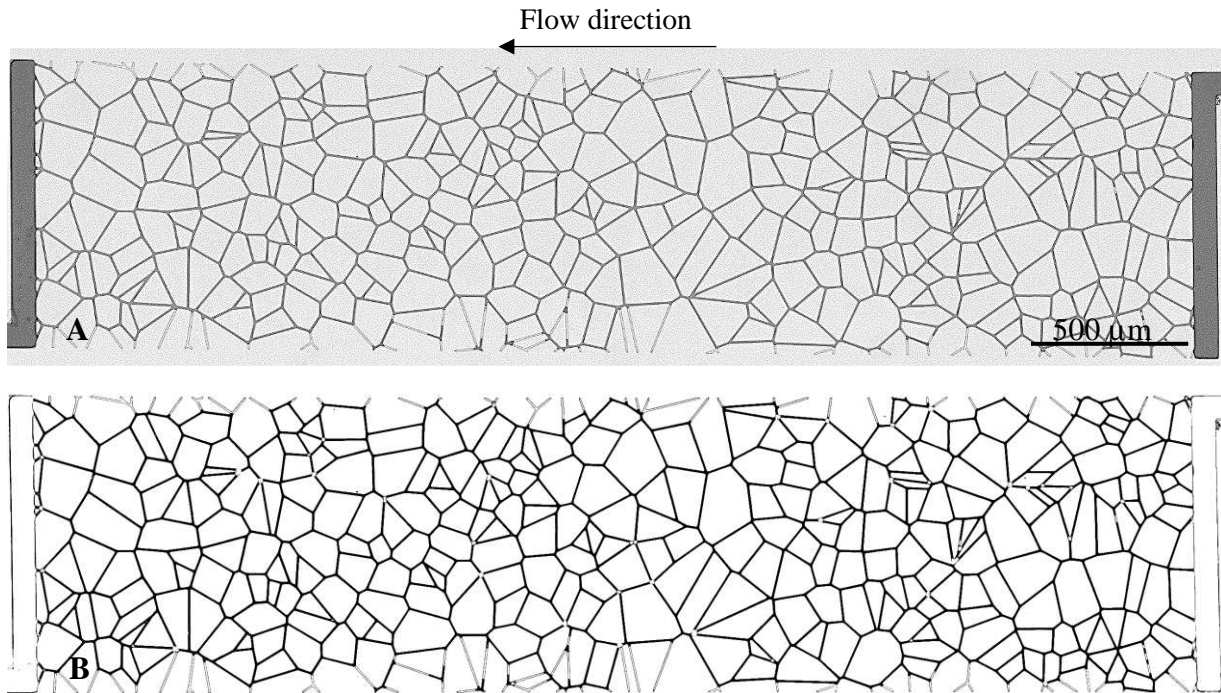


Figure 5.4: Surfactant flooding in water-wet micromodel with degassed crude oil at 10 PV.  
A – Raw image; B – Binary image.

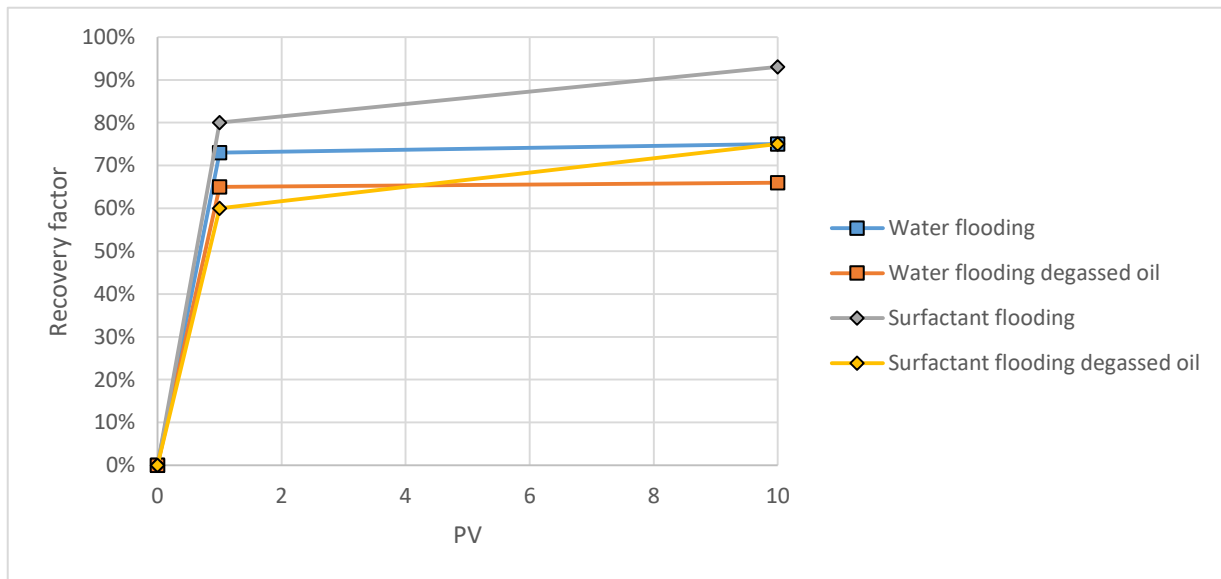


Figure 5.5: Recovery factor in water-wet micromodel.

## 5.2 Displacement in oil-wet micromodels

Figure 5.6 shows distributions of phases in a water flooding experiment carried out in an oil-wet micromodel. Breakthrough took place in 6 seconds with 29% of oil recovery. After 10 PV of additional injection, 32% additional oil recovery was obtained, which is a significant difference when compared to water-wet micromodels. In surfactant flooding, 65% of oil was recovered at breakthrough, which is 15% lower than surfactant flooding in water-wet micromodel. However, more additional oil was produced after breakthrough when compared to water-wet micromodels. The recovery factor at 10 PV was 85% (Figure 5.7). Figure 5.8 and 5.9 show phase distributions of water flooding and surfactant flooding in oil-wet micromodels with degassed crude oil. In water flooding, a single-channel viscous finger developed, and recovery factor at breakthrough was only 13%. 10 PV of additional injection yielded 29% additional oil recovery. In surfactant flooding, recovery factor at breakthrough was 60%, only 5% fewer than that with crude oil. 10 PV of additional injection achieved 71% recovery, which is 14% lower than the case with crude oil. Reduction of IFT, in this case, has significantly improved the displacement efficiency and compensated the effect of unfavorable mobility ratio.

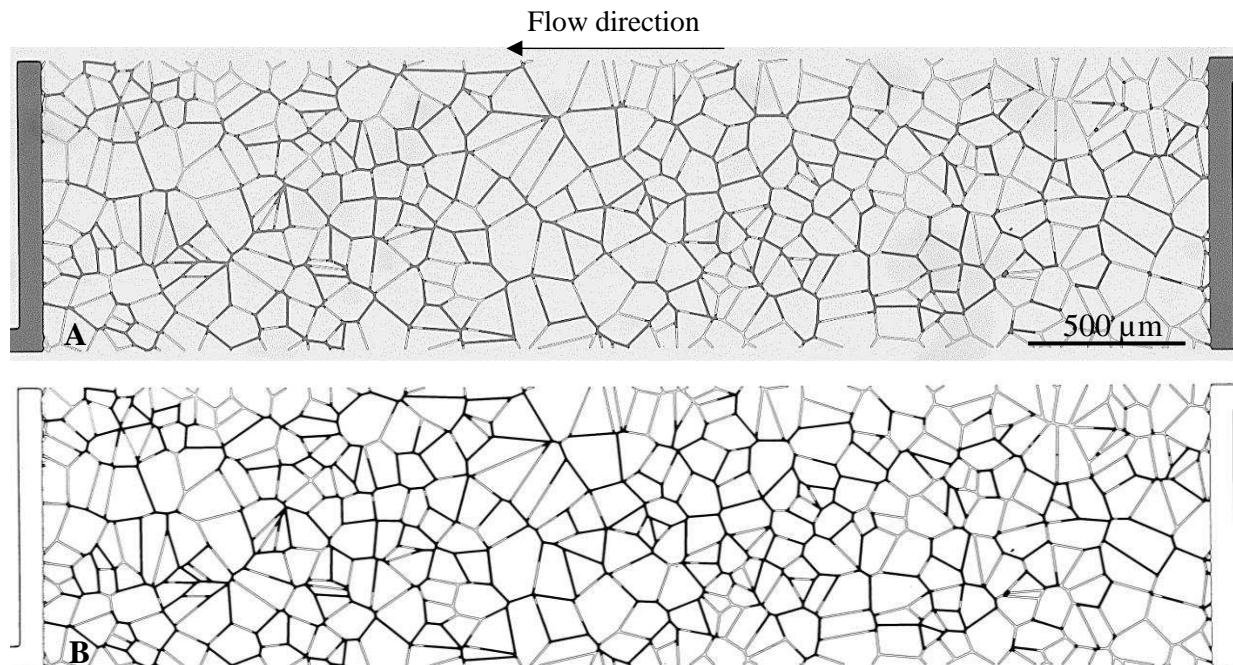


Figure 5.6: Water flooding in an oil-wet micromodel at 10 PV.  
A – Raw image; B – Binary image.



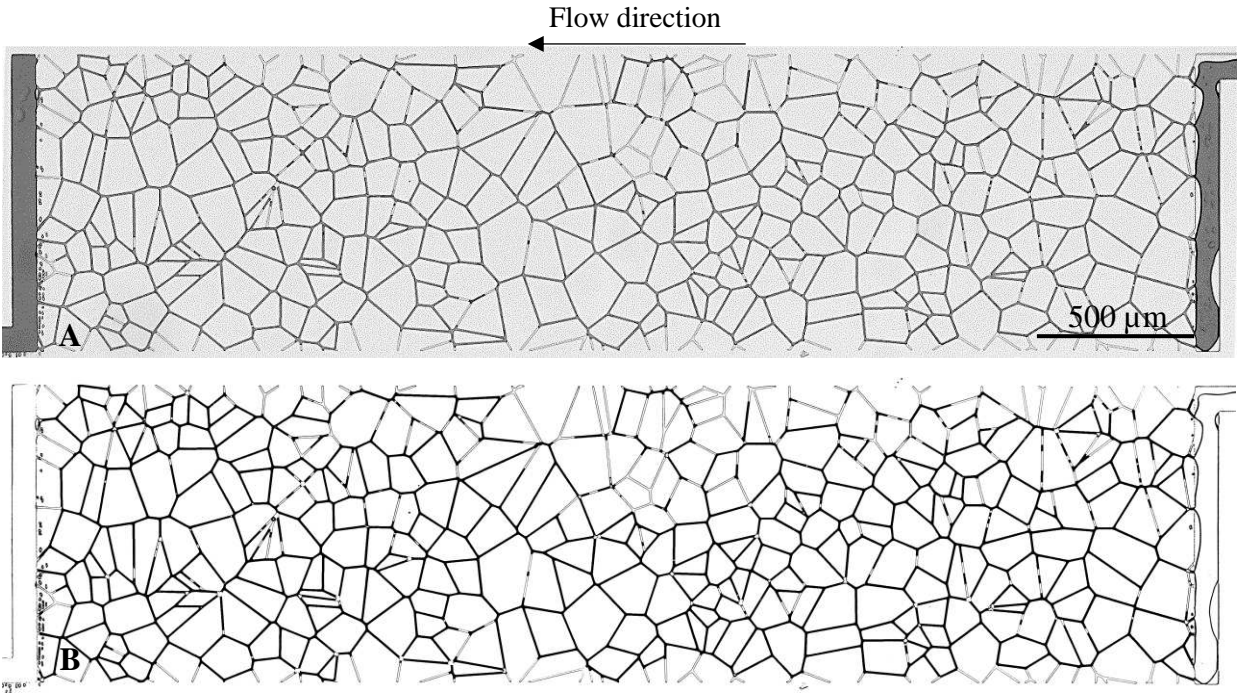


Figure 5.7: Surfactant flooding in an oil-wet micromodel at 10 PV.  
A – Raw image; B – Binary image.

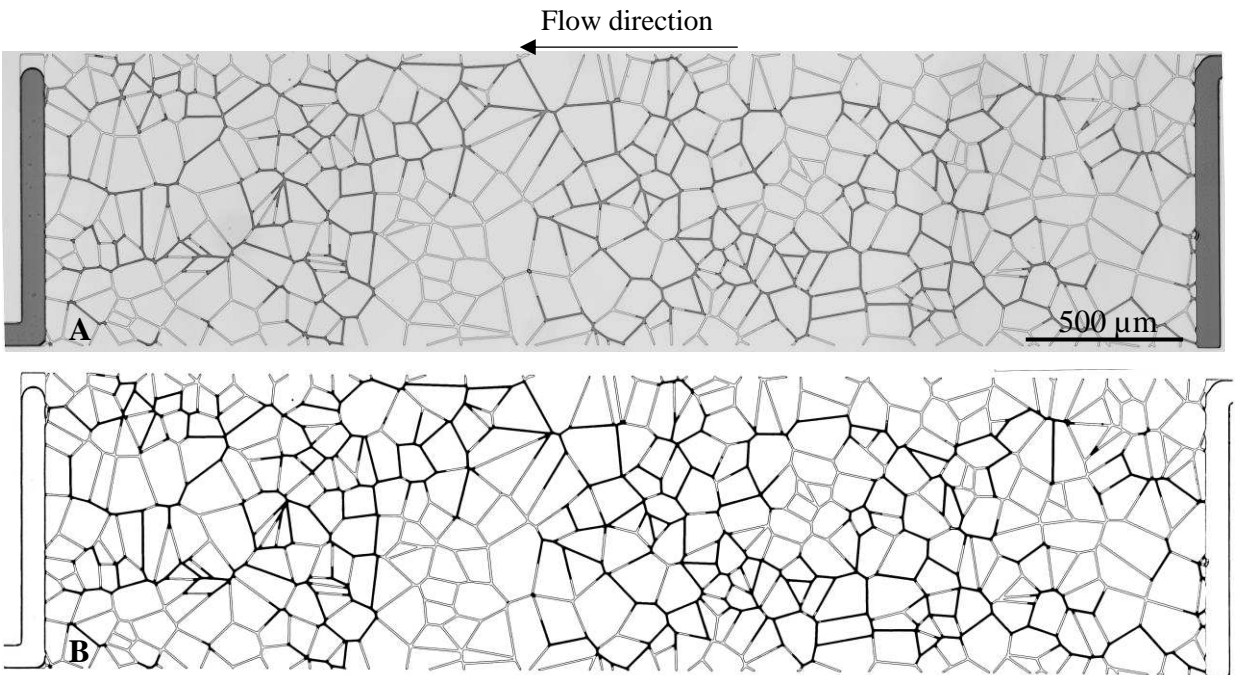


Figure 5.8: Water flooding in an oil-wet micromodel with degassed crude oil at 10 PV.  
A – Raw image; B – Binary image.

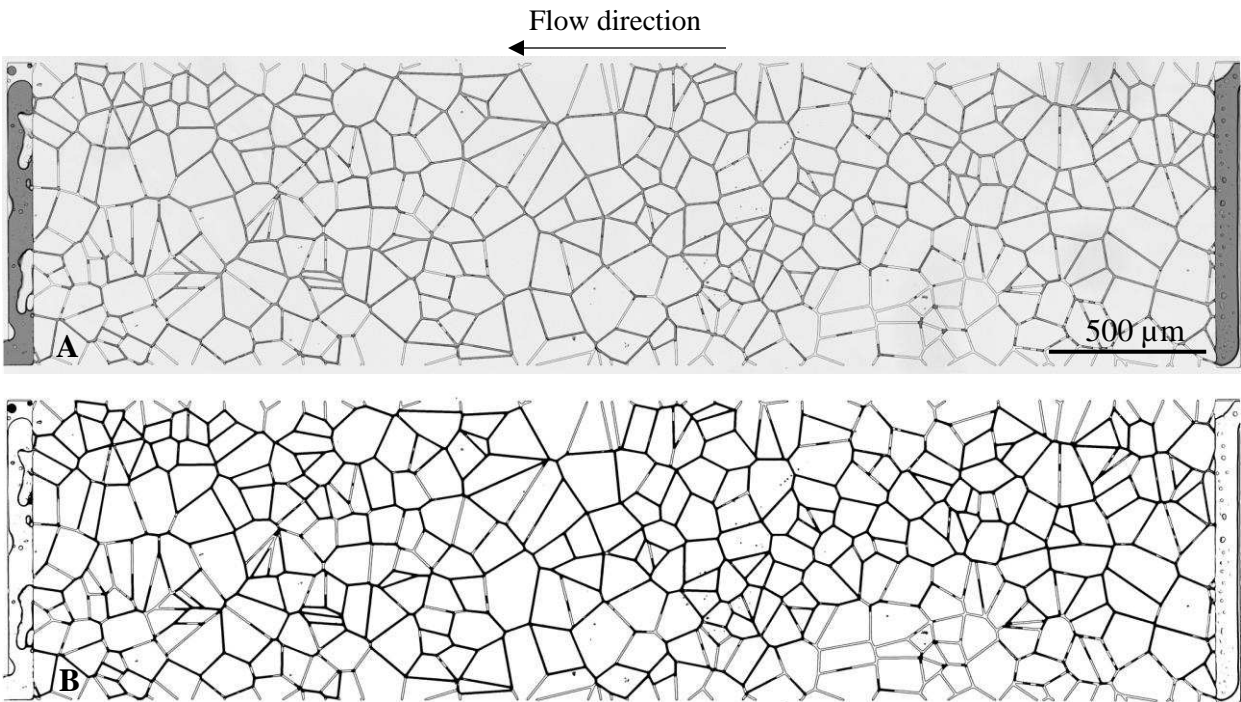


Figure 5.9: Surfactant flooding in an oil-wet micromodel with degassed crude oil at 10 PV.  
A – Raw image; B – Binary image.

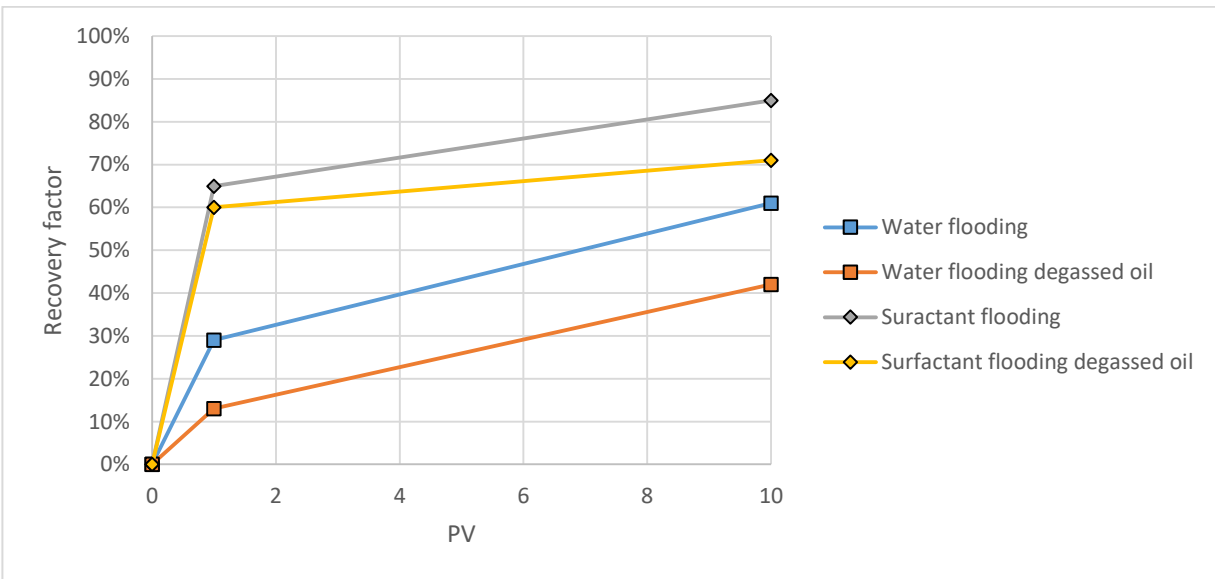


Figure 5.10: Recovery factor in oil-wet micromodel.

### 5.3 Summary

In this chapter, we studied water and surfactant flooding displacement efficiencies in water-wet and oil-wet micromodels. Also, unfavorable mobility ratio condition was investigated by saturating the micromodel with degassed crude oil.

Water-wet micromodels demonstrated high recovery due to the assistance of imbibition of injecting fluid. The breakthrough pattern had a piston like displacement. Although the water-wet micromodels had a high recovery at breakthrough, there was no additional oil produced after breakthrough takes place. In contrast, oil-wet micromodels had fingering breakthrough pattern, which resulted in smaller oil recovery. However, significant additional recovery achieved with more pore volume injected after breakthrough. Surfactant flooding demonstrated a recovery improvement at breakthrough and after breakthrough injection in both water-wet and oil-wet micromodels. However, the surfactant effect was less notable in water-wet micromodels comparing to oil-wet micromodels.

Unfavorable mobility ratio experiments demonstrated that increasing oil viscosity three times dramatically affects oil-wet micromodel recovery efficiency. In oil-wet micromodel water flooding, unfavorable mobility ratio reduced the oil recovery almost three times. However, in water-wet micromodels, the effect of degassed oil only slightly reduced oil recovery. Surfactant flooding improved the recovery in both water-wet and oil-wet micromodels significantly.

It is accepted that water-wet formations are more efficient comparing to oil-wet formations (Mungan 1964). Wettability has a strong effect on relative permeability. In oil-wet core samples, water relative permeability is high, and oil relative permeability is low, which causes early breakthrough and less efficient recovery. In water-wet formations, water tends to imbibe into pores, displacing oil more uniformly (Donaldson et al. 1969). The micromodel flooding results demonstrated good agreement with core flooding experiments. The water-wet micromodel recovery factor was higher than oil-wet micromodel. Also, water-wet micromodel did not produce a notable amount of oil after breakthrough. In contrast, oil-wet micromodel achieved more additional recovery after breakthrough injection. Similar relationship between breakthrough recovery patterns and formation wettability are observed in core flooding experiments too (Anderson 1987).

## CHAPTER 6

### EFFECT OF FRACTURES

Most reservoir rocks contain natural fractures. Natural fractures can form a continuous network, as described by the dual porosity and dual permeability models of fractured porous media (Warren et al. 1963; Kazemi 1969). Alternatively, they can be disconnected, the effect of which on single- and multiphase flows is much less understood. When fractures are present, achieving a high displacement efficiency becomes much more challenging. In this chapter, we investigated two types of fractured porous media to study the effect of fractures on multiphase displacement. The first type contains disconnected fractures and is modeled by the micromodel that is half-fractured (Figure 2.11, B). The second kind includes connected fractures and is modeled by the micromodel that contains a through-fracture in the shape of an “S” (Figure 2.11, C). In addition to the half-fractured and fully-fractured patterns, a homogeneous pattern was added for comparison.

Experiments presented in this chapter are different from those in the previous two chapters in several ways. First, the oil injection step to establish the irreducible water saturation was not carried out due to the difficulty in displacing brine away from the matrix, in particular for the fully-fractured micromodel. Therefore, all experiments started with a fully oil-saturated medium. Secondly, the oil saturation step used -0.08 MPa vacuum for 12 hours to achieve uniform oil saturation in both matrix and fractures. During this period, micromodel wettability becomes preferentially oil wet, and crude oil lost their lighter components and became “degassed”. The viscosity of the degassed crude oil is 13.7 cP at 20 °C. All experiments were conducted with a constant pressure head of 9987 Pa or 1.4 psi. Table 6.1 presents IFT between degassed crude oil and brine/surfactant solution and the corresponding capillary numbers. Micromodel capillary number varies from each other due to the different permeability of each micromodel. The surfactant flooding increased the capillary number for an order of magnitude in all cases.

Table 6.1: Capillary number in water and surfactant flooding

	IFT, [mN/m]	$N_c$ , Water flooding	$N_c$ , Surfactant flooding
Homogeneous pattern	26.6	$6.72 \times 10^{-06}$	$5.41 \times 10^{-05}$
Half-fractured pattern	26.6	$1.34 \times 10^{-05}$	$1.08 \times 10^{-04}$
Fully-fractured pattern	26.6	$1.50 \times 10^{-04}$	$1.21 \times 10^{-03}$

## 6.1 Homogeneous micromodel

Figure 6.1 shows water flooding at 10 PV injected. In the homogeneous micromodel, fingering and quick breakthrough took place. There was 12% additional recovery achieved with 10 PV injected (Figure 6.3). The breakthrough recovery was 21% higher than homogeneous micromodel with degassed crude oil in the previous chapter. The viscosity ratio between two experiments was the same. The main reason for higher recovery could be the difference in wettability between micromodels. Micromodel wettability in this chapter is less oil-wet comparing to APTES treated micromodel, which was used in the previous chapter.

Figure 6.2 shows that the surfactant flooding significantly improved the displacement efficiency. Capillary number increase in one order of magnitude enhanced the recovery for 30% at breakthrough and for 28% at 10 PV. There was 14% additional oil recovery with 10 PV injection.

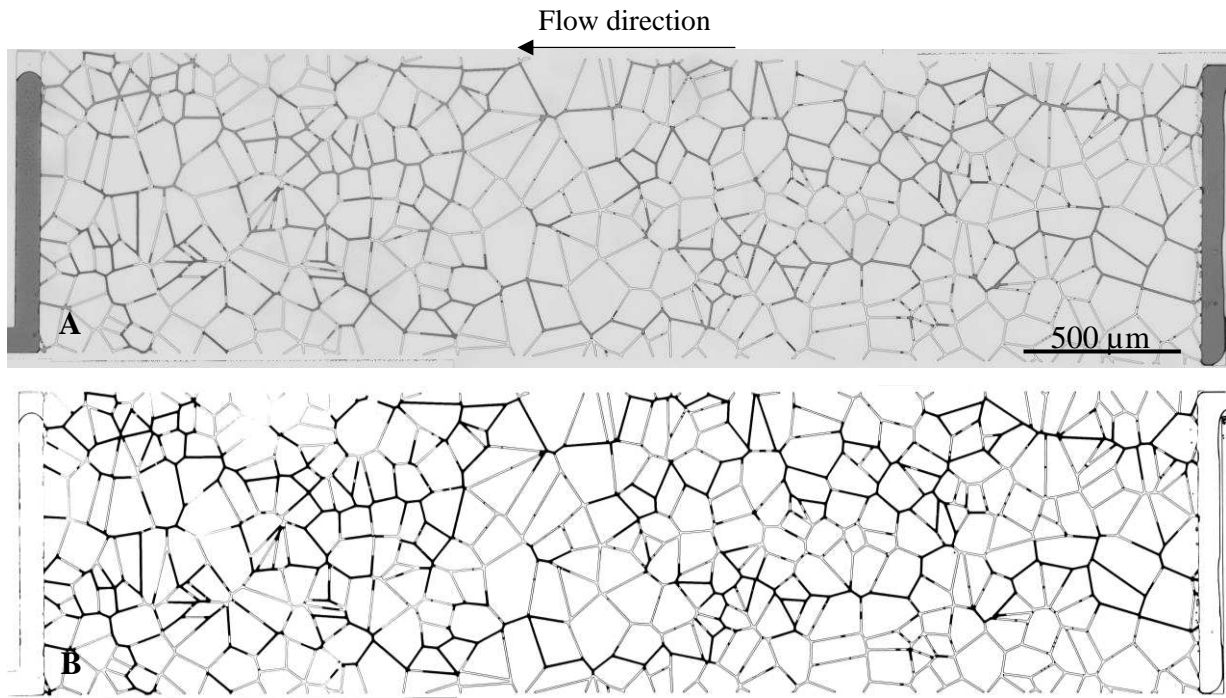


Figure 6.1: Water flooding – Homogeneous pattern. A – Raw image; B – Binary image.

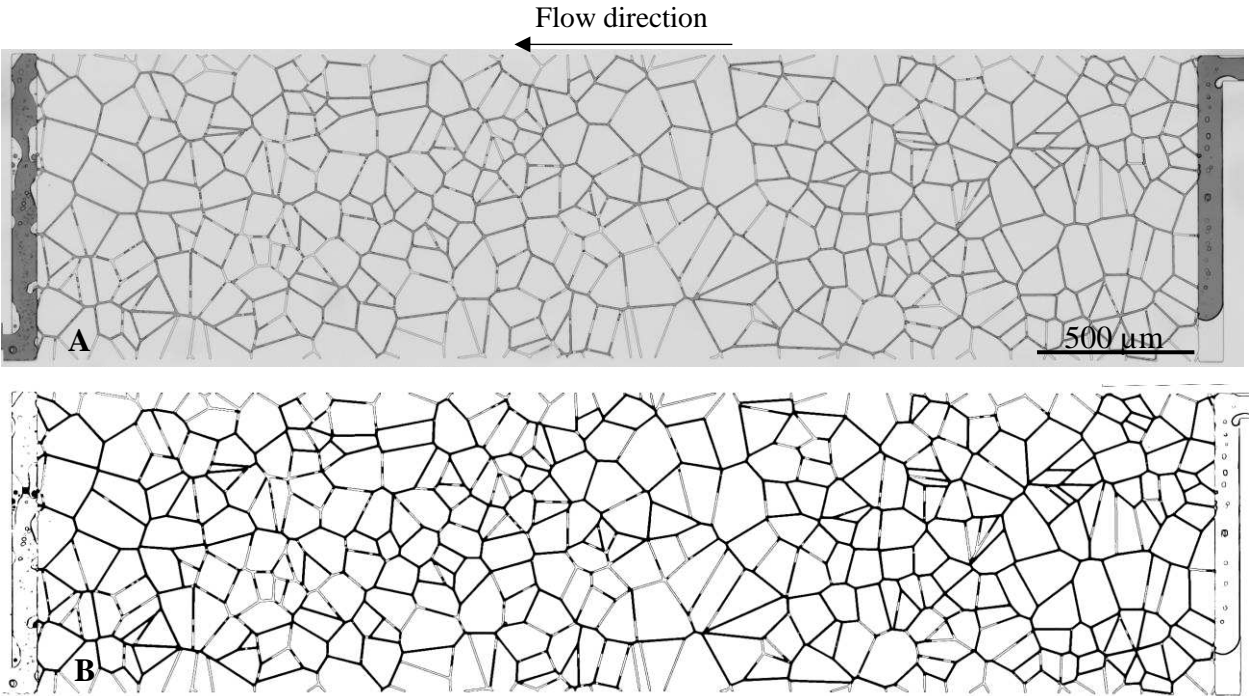


Figure 6.2: Surfactant flooding – Homogeneous micromodel. A – Raw image; B – Binary image.

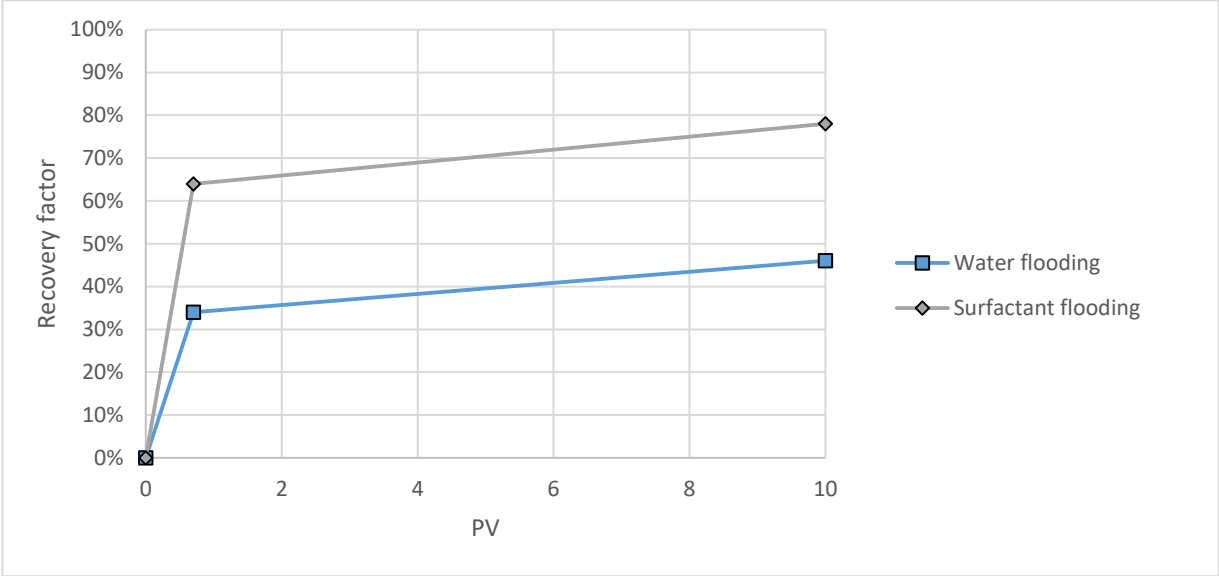


Figure 6.3: Homogeneous micromodel recovery factor as a function of PV injected.

## 6.2 Half-fractured micromodel

Figure 6.4 demonstrates water flooding in half-fractured micromodel. The recovery factor at breakthrough moment was 25%, which is 11% less than in homogeneous micromodel. The reason for the less recovery at breakthrough could be fractures introduced on the sides of the micromodel, which have two times of height and five times of width of the porous media channels. Due to short distance between fractures, the breakthrough time was also much less. In water flooding, 10 PV injection helped to achieve 13% additional recovery.

Figure 6.5 shows that surfactant flooding increased the recovery in half-fractured micromodel greatly. The recovery at breakthrough was 37%, which is 12% higher than in water flooding. Although, it was 27% less than in homogeneous micromodel, after breakthrough, there was 38% additional recovery achieved. Introduction of surfactant in half-fractured reservoir led to almost the same recovery as in homogenous micromodel.

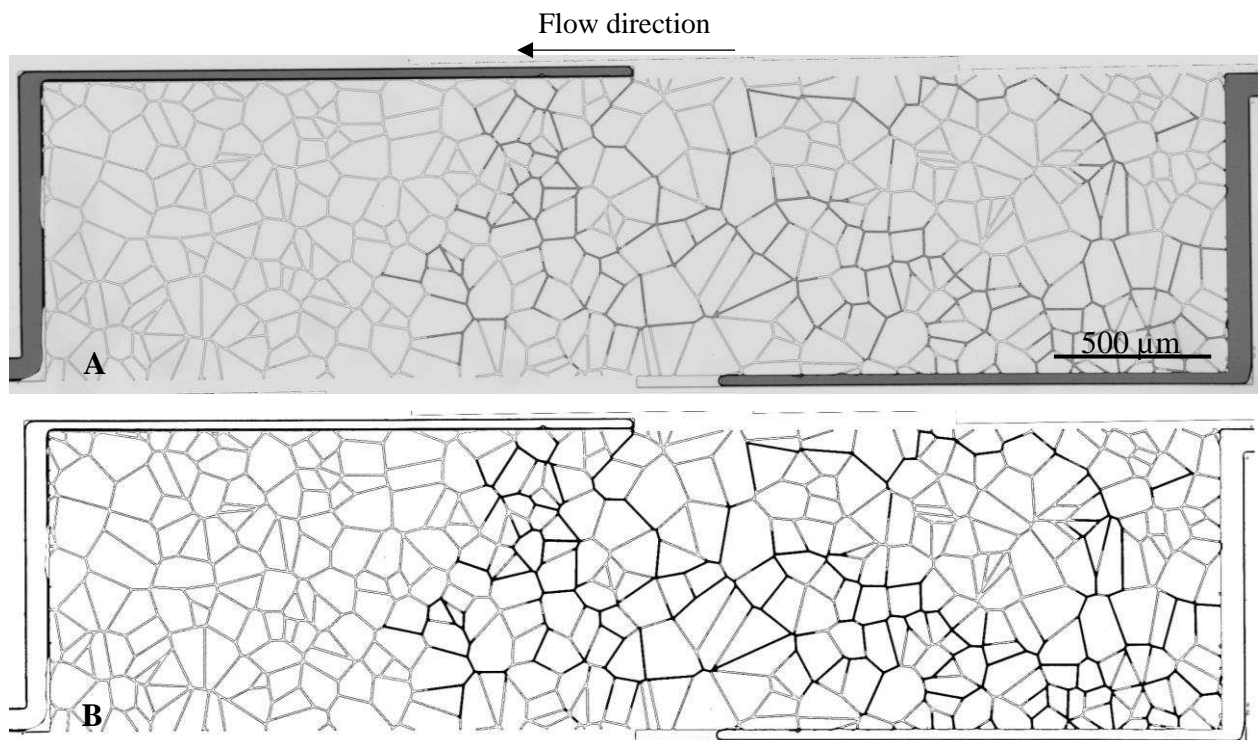


Figure 6.4: Water flooding – Half-fractured pattern. A – Raw image; B – Binary image.

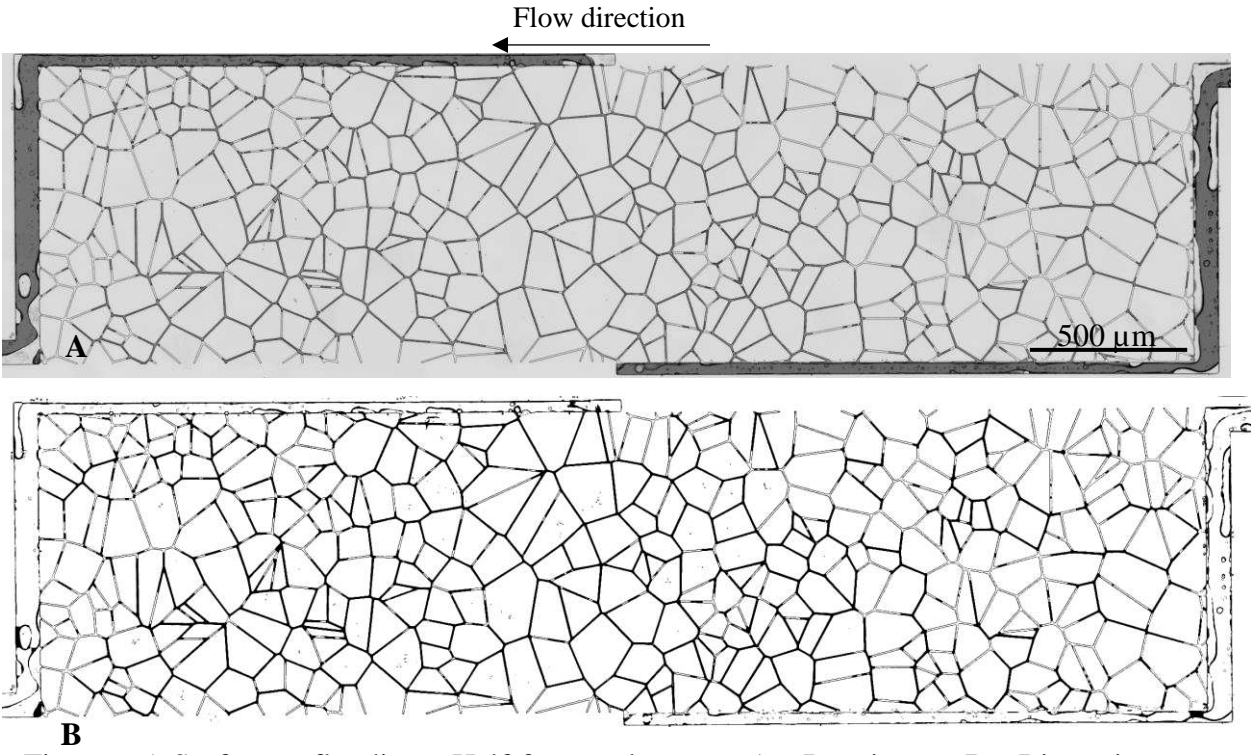


Figure 6.5: Surfactant flooding – Half-fractured pattern. A – Raw image; B – Binary image.

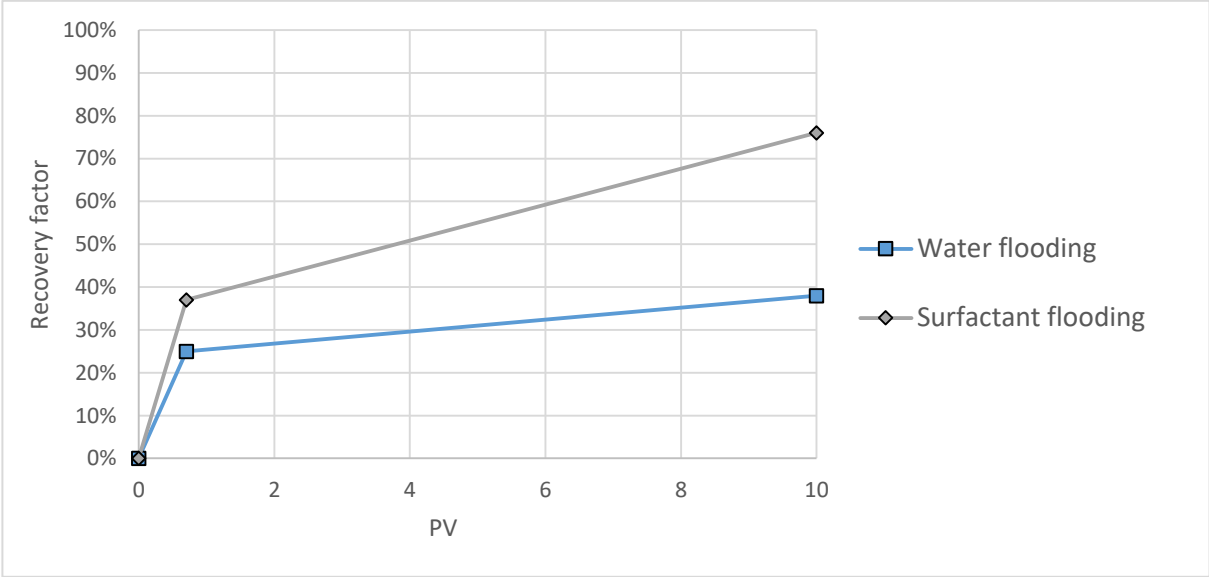


Figure 6.6: Half-fractured micromodel recovery factor as a function of PV injected.



### 6.3 Fully-fractured micromodel

In fully-fractured micromodel, water flooding achieved almost no recovery even at 100 PV injected (Figure 6.7). The pore volume injected is presented in logarithmic scale, because high fluid flow velocity in fractures. Several channels were displaced that gave only 1% recovery. The main reason is the connected fractures that create a highway of fluid flow along the micromodel, and IFT is big enough to keep displacing fluid from penetrating to matrix porosity.

Figure 6.8 demonstrates the surfactant flooding recovery in the fully-fractured micromodel at 100 PV injected. The breakthrough took place in four seconds, and there was no recovery produced at all. After 10 PV injection, 9% oil recovery achieved, which is 28% less than half-fractured micromodel and 55% less than homogenous micromodel. However, IFT reduction by surfactant helped to obtain 82% recovery at 100 PV injected.

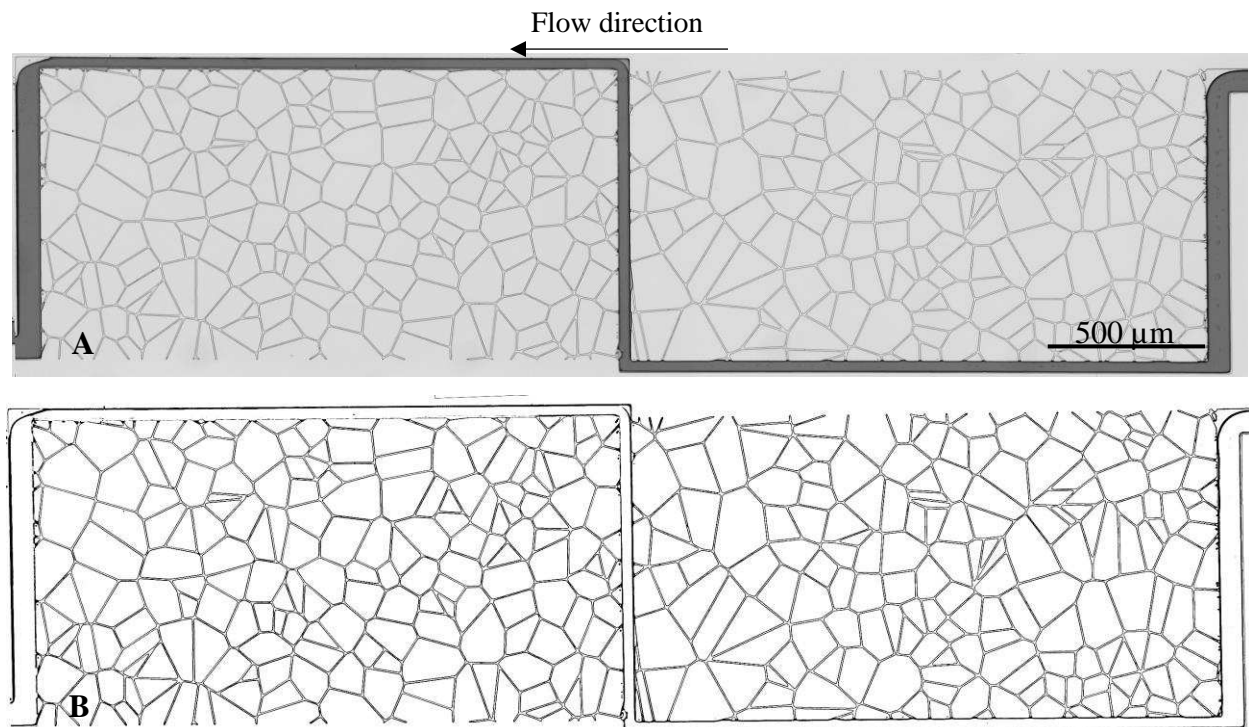


Figure 6.7: Water flooding – Fully fractured micromodel. A – Raw image; B – Binary image.

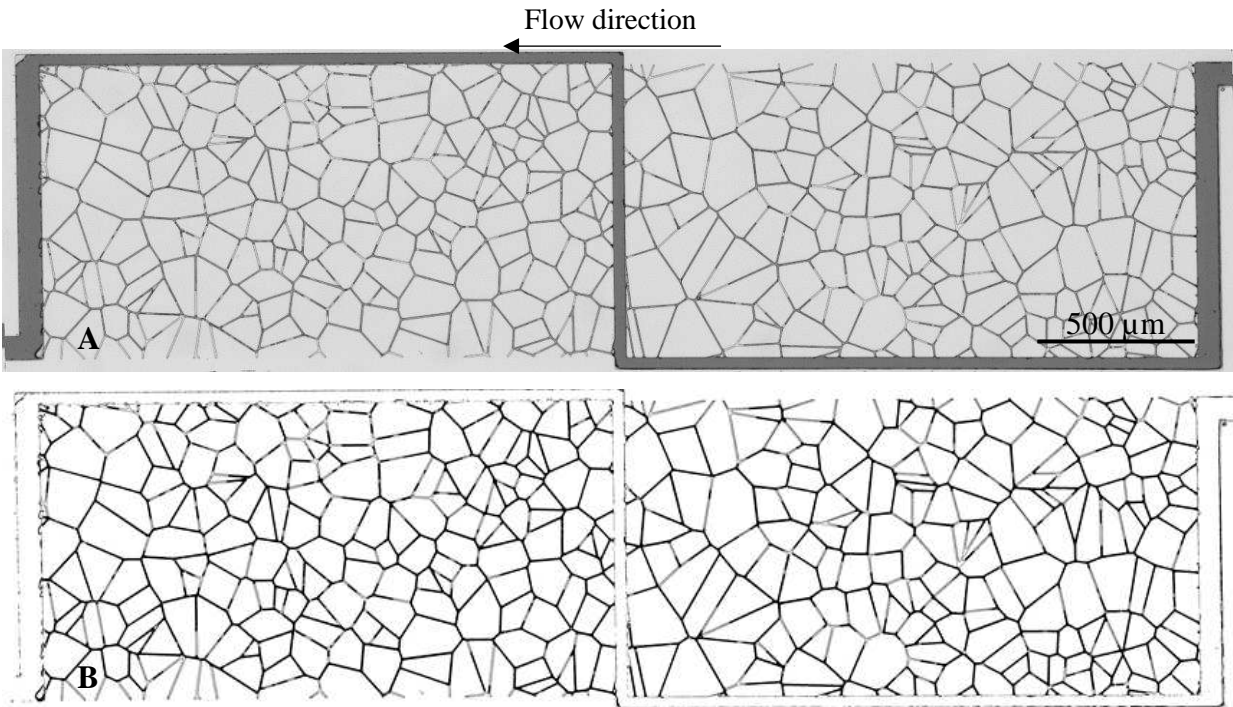


Figure 6.8: Surfactant flooding – Fully fractured micromodel.  
A – Raw image; B – Binary image.

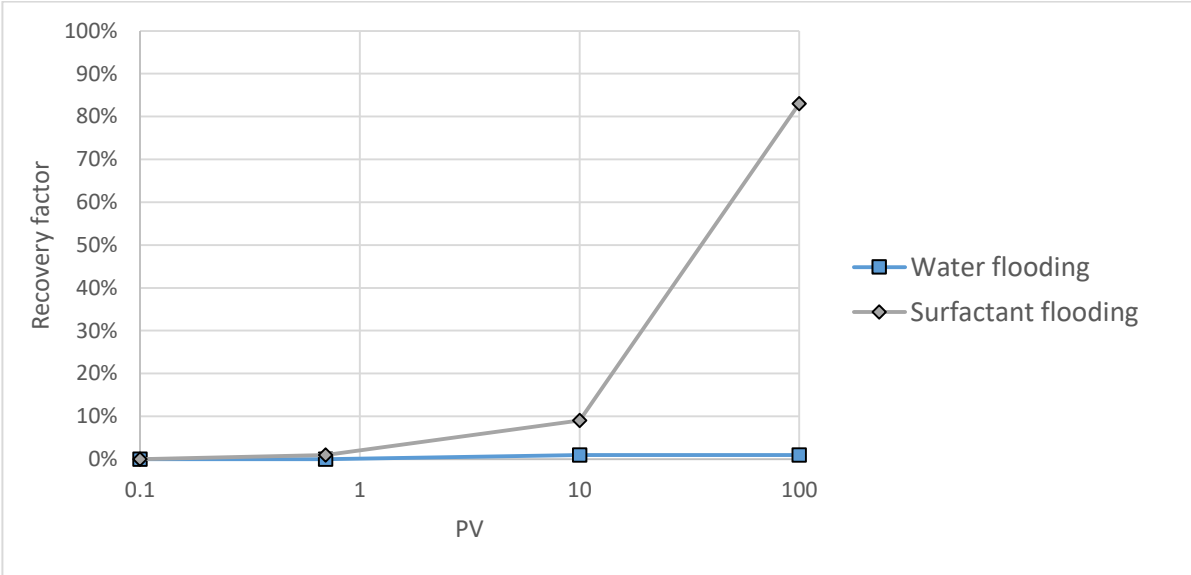


Figure 6.9: Fully fractured micromodel recovery factor as a function of PV injected.

## 6.4 Summary

Compared to homogeneous micromodel, the efficiency of water flooding in half-fractured micromodel is reduced due to partial bypassing, and becomes essentially zero in fully fractured micromodel due to total bypassing of the oil in the matrix. Recovery factor for all three patterns was small, because of unfavorable mobility ratio and introduced fractures. The homogeneous pattern produced 46% at 13.7 cP viscosity comparing to 61% at 4.5 cP viscosity. The half-fractured pattern produced only 38% of the oil. At the same time, fully fractured pattern produced almost nothing. For the homogeneous micromodel, surfactant improved the recovery factor from 46% to 78%. The improvements for half-fractured and full-fractured micromodels, the addition of surfactant turned out to be crucial. In half-fractured micromodel, surfactant flooding helped to improve recovery from 38% to 76% at 10 PV. In case of fully-fractured micromodel, IFT reduction helped to overcome capillary forces related to the size of a pore throat at entry point from fracture to porous media. The surfactant helped to achieve 9% recovery for at 10 PV. After breakthrough, it was required 100 PV injection to reach 81% recovery. Besides, an interesting breakthrough pattern observed. The surfactant solution created small droplets at porous media entrance, which could be formed due to interface instabilities between oil and surfactant solution. Then, the droplets penetrated slowly through porous media. When the droplets reached the middle of porous media, quick and uniform displacement took place.

## CHAPTER 7

### CONCLUSIONS AND RECOMMENDATIONS

#### 7.1 Conclusions

The goal of this thesis work was to fabricate crude oil compatible and high-temperature resistant micromodel to study EOR parameters. Mainly, we wanted to investigate the effects of temperature, IFT, wettability and presence of fractures on displacement efficiency.

We developed procedures to fabricate NOA81 micromodel that allows to modify its wettability and to conduct the experiments at higher temperatures. The oxygen plasma treatment and half-curing methods were combined to obtain highly water-wet surface. In addition, a combination of APTES and half-curing methods provided a highly oil-wet surface. The polymer curing time was also optimized. The bonding strength was excellent in both wettability modification techniques.

The temperature effect demonstrates that the higher temperature reduced IFT slightly, but mobility ratio stayed the same in water flooding. Therefore, the temperature increase did not change the recovery dramatically. In contrast, surfactant flooding achieved high recoveries in both ambient and high temperatures, which implies that the IFT modification is a primary factor affecting the recovery factor.

The wettability experiments show that the water-wet micromodels had high recovery, but almost no additional recovery after breakthrough takes place. In contrast, oil-wet micromodels resulted in lower recovery at breakthrough, however, produced significant oil recovery after breakthrough. Although the surfactant flooding increased the recovery in both cases, IFT reduction was more effective in oil-wet micromodels when compared to water-wet micromodels. In addition, crude oil with different viscosity was tested. The results demonstrated that the unfavorable mobility ratio reduces recovery factor in both water-wet and oil-wet micromodels.

The introduction of fractures in porous media reduced the recovery of micromodels. In water flooding, half-fractured micromodel produced less than homogenous micromodel. The fully-fractured micromodel had no recovery at all. Surfactant flooding helped to improve the recovery significantly in both half-fractured and fully-fractured micromodels. However, the fully-fractured micromodel required more pore volume injection to displace oil from matrix porous media.

Although IFT was a critical parameter in recovery, the mobility ratio improvement could also play a crucial role in displacement efficiency from fractured porous media.

Moreover, interesting phenomena such as microemulsion generation, dead-end pore displacement, and reversal fluid flow in porous media were observed during flooding experiments. These observations could be studied further, which could bring a better understanding of fluid flow dynamics in some oil recovery processes.

## **7.2 Limitations**

The micromodel characteristics such as high precision replication, controllable surface properties and dimensions demonstrate that the micromodels could be used as a standardized screening tool for EOR processes. The displacement efficiency results show that NOA81 micromodel has consistent trends in displacement pattern and recovery factors. However, the results were much higher than real field cases. The small dimensions of micromodel and idealistic porous media pattern could explain such high recoveries. These limitations could be improved introducing various pore throat sizes and increasing sweep area. The real core plug CT scan images could be good example of heterogeneity of pore throat sizes. Also, the NOA81 polymer properties could be investigated more thoroughly, which could provide a better understanding of surface chemistry change with different environments and its effect on wettability. In addition, the experimental setup could be improved to conduct more robust and complex experiments such as high pressure, multiple fluid injection and rock mineralogy introduction.

## **7.3 Recommendations**

In this study, all flooding experiments used the constant pressure of 1.4 psi, created by 1 m brine column, as a driving force. Current experimental setup could be modified to the higher-pressure system. An accurate measurement of pressure difference along the porous media could help to study polymer flooding, scaling and precipitation problems. Also, the real rock powder could be placed in injection tubing before porous media, which will help to account for a mineralogy effect in flooding experiments. Moreover, manipulation of fluids at micro scale could help to investigate the microemulsions generated in porous media. The knowledge of microemulsion fluid properties such as viscosity and density could be extremely helpful in EOR design.

## REFERENCES

- Alvarado, V. and Manrique, E. 2010. Enhanced Oil Recovery: An Update Review. *Energies*, 3(9), 1529-1575; doi:10.3390/en3091529.
- Anderson, W. G. 1987. Wettability Literature Survey-Part 6: The Effects of Wettability on Water flooding. *Journal of Petroleum Technology*, 39(12). SPE-16471-PA. doi:10.2118/16471-PA.
- Atsuyuki, O., Boots, B., Sugihara, K. and Chiu, S. N. 2000. *Spatial Tessellations – Concepts and Applications of Voronoi Diagrams*. Second edition. Wiley, 671.
- Bahari Moghaddam, M. and Rasaei, M. R. 2015. Experimental Study of the Fracture and Matrix Effects on Free-Fall Gravity Drainage with Micromodels. *Journal of Petroleum Technology*, 20(02). SPE-171555-PA. doi:10.2118/171555-PA.
- Bartolo, D., Degre, G., Nghe, P. and Studer, V. 2008. Microfluidic Stickers. *Lab On Chip*, vol. 8, 274-279. doi:10.1039/b712368j.
- Bryant, R. S. and Douglas, J. 1988. Evaluation of Microbial Systems in Porous Media for EOR. *SPE Reservoir Engineers*, 3(02). SPE-16284-PA. doi:10.2118/16284-PA.
- Buchgraber, M., Clemens, T., Castanier, L. M. and Kovscek, A. 2011. A Microvisual Study of the Displacement of Viscous Oil by Polymer Solutions. *SPE Reservoir Evaluation and Engineering*, 14(03). SPE-122400-PA. doi:10.2118/122400-PA.
- Chatenever, A. and Calhoun, J. C. 1952. Visual Examinations of Fluid Behavior in Porous Media - Part I. *Journal of Petroleum Technology*, 4(06). SPE-135-G. doi:10.2118/135-G.
- Childress, G.S. 1975. A Microvisual Study of Initial Displacement of Residual Hydrocarbons by Aqueous Surfactant Solutions. M.Sc. Thesis, University Texas Austin.
- Clemens, T., Tsikouris, K., Buchgraber, M., Castanier, L. M. and Kovscek, A. R. 2012. Pore-Scale Evaluation of Polymers Displacing Viscous Oil – Computational Fluid Dynamics Simulation of Micromodel Experiments. *SPE Improved Oil Recovery Symposium*, 14-18 April, Tulsa, Oklahoma, USA. SPE-154169-MS. doi:10.2118/154169-MS.
- Coates, J. 2000. Interpretation of Infrared Spectra, A Practical Approach. *Encyclopedia of Analytical Chemistry*, 10815-10837.
- Cooke, C. E., Williams, R. E. and Kolodzie, P. A. 1974. Oil Recovery by Alkaline Water flooding. *Journal of Petroleum Technology*, 26(12). 4739-PA. doi:10.2118/4739-PA.
- Cromwell, V., Kortum, D. J. and Bradley, D. J. 1984. The Use of a Medical Computer Tomography (CT) System to Observe Multiphase Flow in Porous Media. *SPE Annual Technical Conference and Exhibition*, 16-19 September, Houston, Texas. SPE-13098-MS. doi:10.2118/13098-MS.

- Danesh, A., Peden, J. M., Krinis, D. and Henderson, G. D. 1987. Pore Level Visual Investigation of Oil Recovery by Solution Gas Drive and Gas Injection. SPE Annual Technical Conference and Exhibition, 27-30 September, Dallas, Texas. SPE-16956-MS. doi:10.2118/16956-MS.
- de Haas, T., Fadaei, H. and Sinton D. 2013. Steam-On-a-Chip for Oil Recovery: The Role of Alkaline Additives in Steam Assisted Gravity Drainage. Lab on a Chip. 13(19), 3832-3839. doi:10.1039/c3lc50612f.
- Donaldson, C., Thomas, D. and Lorenz, B. 1969. Wettability Determination and Its Effect on Recovery Efficiency. Society of Petroleum Engineers Journal, 9(01). SPE-2338-PA. doi:10.2118/2338-PA.
- Duffy, D. C., McDonald, J. C., Anderson, J. R., Chiu, H., Wu, D. T., Schueller, A. and Whitesides, G. M. 1998. Fabrication of Microfluidic Systems in Poly(dimethylsiloxane). Analytical Chemistry, 70(23). doi:10.1021/ac980656z.
- Farzaneh, S. A., Dehghan, A. A., Ghazanfari, M. H. and Kharrat, R. 2012. A Comparative Study on WAS, SWAS, and Solvent-Soak Scenarios Applied to Heavy-Oil Reservoirs Using Five-Spot Glass Micromodels. Journal of Canadian Petroleum Technology, 51(06). SPE-158376-PA. doi:10.2118/158376-PA.
- Gale, W. W. and Sandvik, E. I. 1973. Tertiary Surfactant Flooding: Petroleum Sulfonate Composition-Efficacy Studies. Society of Petroleum Engineers Journal, 13(04). doi:10.2118/3804-PA.
- Green, D. and Willhite, P. 1998. Enhanced Oil Recovery. Society of Petroleum Engineers Monograph. Chapter 6, 186-239.
- Gunda, N.S.K., Bera, B., Karadimitriou, N.K., Mitra, S.K. and Hassinazadeh, S.M. 2011. Reservoir-on-Chip (ROC): A New Paradigm in Reservoir Engineering. Lab on Chip, 11(22), 3785-3792. doi:10.1039/c1lc20556k.
- Guo, H., Zitha, P. L. J., Faber, R. and Buijse, M. 2012. A Novel Alkaline/Surfactant/Foam Enhanced Oil Recovery Process. Society of Petroleum Engineers Journal, 17(04). SPE-145043-PA. doi:10.2118/145043-PA.
- He, K., Xu, X., Gao, Y., Yin, X. and Neeves, K. B. 2015. Evaluation of Surfactant Performance in Fracturing Fluids for Enhanced Well Productivity in Unconventional Reservoirs Using Rock-on-a-Chip Approach. Journal of Petroleum Science and Engineering. 135, 531-541. <http://dx.doi.org/10.1016/j.petrol.2015.10.008>.
- Hempkins, W. B., Massey, G. R. and Timur, A. 1971. Analysis of Sidewell Samples By Nuclear Magnetic Resonance Methods. Society of Petrophysicists and Well-Log Analysts. 12(06).
- Howe, A. M., Clarke, A., Mitchell, J., Staniland, J. and Hawkes, L. A. 2015. Visualizing Surfactant EOR in Core Plugs and Micromodels. SPE Asia Pacific Enhanced Oil Recovery Conference, 11-13 August, Kuala Lumpur, Malaysia. SPE-174643-MS. doi:10.2118/174643-MS.

- Hoyle, C. E. and Bowman, C. N. 2010. Thio-Ene Click Chemistry. *Angewandte Chemie Int.*, (49), 1540-1573.
- Javadpour, F. and Fisher, D. 2008. Nanotechnology-Based Micromodels and New Image Analysis to Study Transport in Porous Media. *Journal of Canadian Petroleum Technology*, 47(2) doi:10.2118/08-02-30.
- Kazemi, H. 1969. Pressure Transient Analysis of Naturally Fractured Reservoirs with Uniform Fracture Distribution. *Society of Petroleum Engineers Journal*, 9(04). SPE-2156-A. doi:10.2118/2156-A.
- Levachee, B., Azione, A., Bourrel, M., Studer, V. and Bartolo, D. 2012. Engineering the Surface Properties of Microfluidic Stickers. *Lab on Chip*, vol.12, 3028-3031. doi:10.1039/c2lc40284j.
- Lin, B. J. 2009. *Optical Lithography*. SPIE Press. Bellingham, WA, 136.
- Manlowe, D. J. and Radke, C. J. 1990. A Pore-Level Investigation of Foam/Oil Interactions in Porous Media. *SPE Reservoir Engineering*, 5(04). SPE-18069-PA. doi:10.2118/18069-PA.
- Mirzaei, M., DiCarlo, D. A. and Pope, G. 2015. Visualization and Analysis of Surfactant Imbibition into Oil-Wet Fractured Cores. *Society of Petroleum Engineers Journal*, 21(01). SPE-166129-PA. doi:10.2118/166129-PA.
- Molla, S. and Mostowfi, F. 2014. Microfluidic Platform for PVT Measurements. *SPE Annual Technical Conference and Exhibition*, 27-29 October, Amsterdam, The Netherlands. SPE-170910-MS. doi:10.2118/170910-MS.
- Mungan, N. 1964. Role of Wettability and Interfacial Tension in Water Flooding. *Society of Petroleum Engineers Journal*, 4(02). SPE-705. <http://dx.doi.org/10.2118/705-PA>.
- Nelson, H. P. 2009. Pore-Throat Sizes in Sandstones, Tight Sandstones, and Shales. *American Association of Petroleum Geologists Bulletin*, (93)3. doi:10.1306/10240808059.
- Nguyen, P., Fadaei, H. and Sinton, D. 2014. Pore-scale Assessment of Nanoparticle Stabilized CO<sub>2</sub> Foam for Enhanced Oil Recovery. *Energy and Fuels*, 28(10), 6221–6227. doi:10.1021/ef5011995.
- Rangel-German, E. R. and Kovscek, A. 2006. A Micromodel Investigation of Two-Phase Matrix-Fracture Transfer Mechanisms. *Water Resources Research*, 42(3). doi:10.1029/2004WR003918.
- Romero-Zeron, L. B., and Kantzas, A. 2007. The Effect of Wettability and Pore Geometry on Foamed-Gel-Blockage Performance. *SPE Reservoir Evaluation and Engineering*, 10(02). SPE-89388-PA. doi:10.2118/89388-PA.
- Shokrlu, H. Y. and Babadagli, T. 2015. Pore-Scale Investigation of Phase Distribution and Residual-Oil Development During Secondary and Tertiary Solvent Injection. *SPE Reservoir Evaluation and Engineering*, 18(01). SPE-173180-PA. doi:10.2118/173180-PA.



- Silvestrini, S., Ferraro, D., Tóth, T., Pierno, M., Carofiglio, T., Mistura G. and Maggini, M. 2012. Tailoring the Wetting Properties of Thiolene Microfluidic Materials. *Lab Chip*, 12, 4041-4043. doi:10.1039/C2LC40651A.
- Sinton, D. 2014. Energy: The Microfluidic Frontier. *Lab on a Chip*. 14(17), 3127-3134. doi:10.1039/c4lc00267a.
- Song, W. and Kovscek, A. R. 2015. Functionalization of Micromodels with Kaolinite for Investigation of Low Salinity Oil-Recovery Processes. *Lab on a chip*. 15(16), 3314-3325. doi:10.1039/c5lc00544b.
- Syed, A. H., Mosavat, N., Riordon, J., Lele, P., Qi, Z., Kim, M., Fadaei, H., Guerrero, A. and Sinton, D. 2016. A Combined Method for Pore-Scale Optical and Thermal Characterization of SAGD. *Journal of Petroleum Science and Engineering*, vol.146, 866-873. doi:10.1016/j.petrol.2016.07.030.
- Tong, Z., Yang, C., Wu, G., Yuan, H., Yu, L. and Tian, G. 1998. A Study of Microscopic Flooding Mechanism of Surfactant/Alkali/Polymer. SPE/DOE Improved Oil Recovery Symposium, 19-22 April, Tulsa, Oklahoma. SPE-39662-MS. doi:10.2118/39662-MS.
- Wagli, P., Guelat, B., Homsy, A. and Rooij, N. 2010. Microfluidic Devices Made of UV-Curable Glue (NOA81) for Fluorescence Detection Based Applications. 14<sup>th</sup> International Conference on Miniaturized Systems for Chemistry and Life Sciences. 3-7 October, Groningen, the Netherlands.
- Wagli, P., Homsy, A. and de Rooij, N. F. 2011. Norland Optical Adhesive (NOA81) Microchannels with Adjustable Wetting Behavior and High Resistance Against a Range of Mid-Infrared-Transparent Organic Solvents. *Sensors and Actuators B Chemical*. doi:10.1016/j.snb.2011.02.005.
- Wang, L., Parsa, E., Gao, Y., Ok, J. T., Neeves, K., Yin, X. and Ozkan, E. 2014. Experimental Study and Modeling of the Effect of Nanoconfinement on Hydrocarbon Phase Behavior in Unconventional Reservoirs. SPE Western North American and Rocky Mountain Joint Meeting, 17-18 April, Denver, Colorado. SPE-169581-MS. doi:10.2118/169581-MS.
- Warren, J.E. and Root, P.J. 1963. The Behavior of Naturally Fractured Reservoirs. *Society of Petroleum Engineers Journal*, 3(3), 245-255. <http://dx.doi.org/10.2118/426-PA>.
- Wu, M., Xiao F., Johnson-Paben, R. M., Retterer, S. T., Yin X. and Neeves, K. 2012. Single- and Two-Phase Flow in Microfluidic Porous Media Analogs Based on Voronoi Tessellation. *Lab Chip*. 12(2), 253-61. doi:10.1039/c1lc20838a.
- Wu, Q., Bai, B., Ma, Y., Ok, J. T., Yin, X. and Neeves, K. 2014. Optic Imaging of Two-Phase-Flow Behavior in 1D Nanoscale Channels. *Society of Petroleum Engineers Journal*, 19(05). SPE-164549-PA. doi:10.2118/164549-PA.

- Xu, W., Ok, J. T., Xiao, F., Neeves, K. B. and Yin, X. 2014. Effect of Pore Geometry and Interfacial Tension on Water-Oil Displacement Efficiency in Oil-Wet Microfluidic Porous Media Analogs. *Physics of Fluids*, 26. doi:10.1039/c1lc20838a.
- Yousef, A. A., Al-Saleh, S. H., Al-Kaabi, A. and Al-Jawfi, M. S. 2011. Laboratory Investigation of the Impact of Injection-Water Salinity and Ionic Content on Oil Recovery from Carbonate Reservoirs. *SPE Reservoir Evaluation and Engineering*, 14(05). SPE-137634-PA. doi:10.2118/137634-PA.
- Zeilinger, S., McNeil, R. I., Belkin, A., Brasseur, M., Rosoff, M., Gentalen, E. and Spaid, M. 2003. Use of Microfluidic Devices to Investigate Formation Damage. *SPE European Formation Damage Conference*, 13-14 May, The Hague, Netherlands. SPE-82200-MS. doi:10.2118/82200-MS.